

Cosmological simulations of black hole growth: AGN luminosities and downsizing

Michaela Hirschmann^{1*}, Klaus Dolag^{2,3}, Alexandro Saro², Stefano Borgani^{1,4,5},
Andreas Burkert^{2,6}

¹*INAF - Astronomical Observatory of Trieste, via G.B. Tiepolo 11, I-34143 Trieste, Italy*

²*Universitäts Sternwarte München, Scheinerstr.1, D-81679 München, Germany*

³*Max-Planck-Institute für Astrophysik, Karl-Schwarzschild Strasse 1, D-85740 Garching, Germany*

⁴*Astronomy Unit, Department of Physics, University of Trieste, via G.B. Tiepolo 11, I-34131 Trieste, Italy*

⁵*INFN-National Institute for Nuclear Physics, Via Valerio 2, I-34127 Trieste, Italy*

⁶*Max-Planck-Institut für extraterrestrische Physik (MPE), Giessenbachstr. 1, 85748 Garching, Germany*

Accepted ???. Received ??? in original form ???

ABSTRACT

In this study, we present a detailed, statistical analysis of black hole growth and the evolution of active galactic nuclei (AGN) using cosmological hydrodynamic simulations run down to $z = 0$. The simulations self-consistently follow radiative cooling, star formation, metal enrichment, black hole growth and associated feedback processes from both supernovae typeII/Ia and AGN. We consider two simulation runs, one with a large co-moving volume of $(128 \text{ Mpc/h})^3$ and one with a smaller volume of $(48 \text{ Mpc/h})^3$ but with a by a factor of almost 20 higher mass resolution. We compare the predicted statistical properties of AGN with results from large observational surveys. Consistently with previous results, our simulations are in reasonably good agreement with black hole properties of the local Universe. Furthermore, our simulations can successfully reproduce the evolution of the bolometric AGN luminosity function for both the low-luminosity and the high-luminosity end up to $z = 2.5$. In particular, the latter is for the first time accessible thanks to the large simulated volume in our larger run. In addition, the smaller but higher resolution run is able to match the observational data of the low bolometric luminosity end up to $z = 4 - 5$. We also perform a direct comparison with the observed soft and hard X-ray luminosity functions of AGN, including an empirical correction for a torus-level obscuration, and find a similarly good agreement. These results show that our simulations can self-consistently predict the observed “downsizing” trend in the AGN number density evolution, i.e. the number densities of luminous AGN peak at higher redshifts than those of faint AGN. Implications of the downsizing behaviour on active black holes, their masses and Eddington-ratios are discussed. Overall, the downsizing behaviour in the AGN number density as a function of redshift can be attributed to a combination of the gas density evolution in the resolved vicinity of a (massive) black hole (which is depleted with evolving time mainly as a consequence of the radio-mode feedback) and to the decreasing mean relative velocities between the (low mass) black holes and the surrounding gas with decreasing redshift.

Key words: galaxies: active, galaxies: evolution, galaxies: formation, galaxies: nuclei, quasars: general, methods: numerical

1 INTRODUCTION

It is now generally accepted that present-day spheroidal galaxies host supermassive black holes at their centres (Magorrian et al. 1998; Genzel & Eckart 1999).

In addition, strong correlations have been found between black hole masses and properties of their host galaxies (Ferrarese & Merritt 2000; Gebhardt et al. 2000; Tremaine et al. 2002; Häring & Rix 2004; Graham & Driver 2007; Gültekin et al. 2009; Burkert & Tremaine 2010; McConnell & Ma 2013) as the bulge mass, the stellar velocity dispersion, the Sersic index or the number of

* E-mail: mhirsch@oats.inaf.it

globular clusters. This can be interpreted as an evidence for a co-evolution between the host galaxies and their black holes. Note that a recent study of Kormendy & Ho (2013) gives an up-to-date review about new results in which black holes correlate differently with different galaxy components and about their implications on the co-evolution of galaxies and black holes. These relations have also been shown to possibly have a “non-causal” origin and thus, may be just a consequence of statistical merging processes (Peng 2007; Hirschmann et al. 2010; Jahnke & Macciò 2011). In addition, some recent observations of black hole growth and star formation in individual objects appear to contradict the picture of a simple one-to-one co-evolution over time (e.g. Mullaney et al. 2012; Bongiorno 2012; Rosario 2012). Thus, the details of black hole and galaxy co-evolution remain an unresolved puzzle. During their lifetime, black holes are assumed to undergo several episodes of significant gas accretion, during which this accretion powers luminous quasars or active galactic nuclei (AGN) (Salpeter 1964; Zel’Dovich 1964; Lynden-Bell 1969). By estimating the total energy radiated by AGN over their whole lifetime, it can be shown that nearly all the mass seen in dormant black holes today can be accumulated during the periods of observed bright AGN activity (Soltan 1982). This implies that there is not much room left for “dark” or obscured accretion.

Interestingly, all observational studies of AGN in the hard and soft X-ray range (XMM-Newton, Chandra, ROSAT, ASCA, e.g. Miyaji et al. 2000; La Franca et al. 2002; Cowie et al. 2003; Fiore et al. 2003; Barger et al. 2003; Ueda et al. 2003; Hasinger et al. 2005; Barger & Cowie 2005; Sazonov & Revnivtsev 2004; Nandra et al. 2005; Ebrero et al. 2009; Aird et al. 2010; Fiore et al. 2012) have revealed a possibly on first sight puzzling behaviour of AGN concerning the evolution of the co-moving number density of AGN: the number density of successively more luminous AGN peaks at higher redshifts than the one of less luminous AGN, with the lowest luminosity AGN showing an almost constant co-moving number density. Making the simplified (and naive) assumption that AGN luminosity (i.e. black hole accretion) is proportional to black hole mass (which we would expect if black holes are accreting at the Eddington rate, $L \propto M_{\bullet}$) would imply that very massive black holes seem to be already in place at very early times, whereas less massive black holes seem to evolve predominantly at lower redshifts. This behaviour is called “downsizing” or “anti-hierarchical” growth of black holes. The downsizing trend is also seen in the optical (Cristiani et al. 2004; Croom et al. 2004; Fan et al. 2004; Hunt et al. 2004; Richards et al. 2006; Wolf et al. 2003) and the near-infrared (NIR) (e.g. Matute et al. 2006). This observational result seems to be in conflict with the “naive” expectations arising from the currently favoured hierarchical structure formation paradigm based on the Cold Dark Matter (CDM) model (Peebles 1965; White & Rees 1978; Blumenthal et al. 1985). In this framework, low mass halos are expected to form first and more massive halos to grow later over time via subsequent merging and smooth accretion.

To explore the formation and evolution of black holes and AGN, a large amount of studies have been published based on semi-analytic models of galaxy formation

within which mechanisms for black hole formation and evolution have been included (e.g. Kauffmann & Haehnelt 2000; Volonteri et al. 2003; Granato et al. 2004; Menci et al. 2004; Bromley et al. 2004; Monaco & Fontanot 2005; Croton 2006; Bower et al. 2006; Marulli et al. 2008; Somerville et al. 2008; Bonoli et al. 2009; Fanidakis et al. 2012; Hirschmann et al. 2012; Neistein & Netzer 2013; Menci et al. 2013). It has been shown by some of the above studies that an anti-hierarchical behaviour can be explained within a hierarchical structure formation scenario (Marulli et al. 2008; Bonoli et al. 2009; Fanidakis et al. 2012; Hirschmann et al. 2012; Menci et al. 2013), when considering different models for black hole accretion and AGN triggering and/or accounting for dust obscuration. Unfortunately, these different models have not been able to draw a completely uniform picture for the origin of the downsizing behaviour as they differ in many details.

In addition to these semi-analytic models, also a large number of other studies have investigate the predictions of the cosmological Λ CDM model for the formation and evolution of super-massive black holes (SMBH) and AGN. Some works made predictions based on nearly purely analytic models (Efstathiou & Rees 1988; Haehnelt & Rees 1993; Haiman & Loeb 1998) and on semi-empirical models (Shankar et al. 2009, 2010, 2012). Several years ago, numerical hydrodynamic simulations of isolated galaxy mergers have started to include prescriptions for black hole growth and AGN feedback using “sub-grid” recipes, where black hole accretion according to the Bondi-Hoyle-Littleton formula was assumed (Springel et al. 2005a; Hopkins et al. 2006; Di Matteo et al. 2005; Robertson et al. 2006; Li et al. 2007; Sijacki et al. 2007; Johansson et al. 2009 and references therein). Hopkins et al. (2008), for example, presented predictions based on “semi-empirical” models in which galaxy properties were taken from observations and the relationship between galaxy properties and AGN luminosity was based on the results of a large suite of hydrodynamic merger simulations.

All these models (i.e. analytic, semi-analytic and hydrodynamic simulations) differ in many of the details of how black hole formation and growth are implemented, but there seems to be a broad consensus on several points. First, a self-regulated black hole growth, perhaps via radiation pressure driven winds (Di Matteo et al. 2005; King 2005; Murray et al. 2005; Robertson et al. 2006) is widely adopted to be responsible for obtaining the observed tight relationship between black hole mass and spheroid mass (although some models simply assume this relationship without invoking a physical mechanism). Second, one needs a physical mechanism for AGN triggering that can bring large amounts of gas to the central black hole within a short time. Motivated by hydrodynamic simulations, galaxy-galaxy mergers are a popular (though not universally adopted) way to remove angular momentum from the gas due to gravitational tidal fields and efficiently drive it to the centre of the galaxy. In addition, secular evolution disk instabilities may have a similar effect as (minor) merger events and have been particularly discussed to trigger moderately luminous AGN (see e.g. Hirschmann et al. 2012; Gabor & Bournaud 2013). Third, a mechanism should be included that reduces or stops gas cooling and accretion in massive dark matter halos (to overcome the so-called

“over-cooling” problem). Many models assume that low levels of accretion onto super-massive black holes can produce radio jets that heat the surrounding hot halo gas and/or can drive momentum-mechanically outflows (Croton 2006; Bower et al. 2006; Sijacki et al. 2007; Somerville et al. 2008; Fabjan et al. 2010; Debuhr et al. 2012; Choi et al. 2012; Barai et al. 2013) thereby inhibiting cooling flows and preventing over-massive galaxies from forming and efficiently quenching star formation in massive galaxies.

However, several aspects of the physics of black hole growth and formation remain poorly understood. First, there are active ongoing debates about when and how seed black holes form: either via a direct collapse of cold gas clouds leading to massive seeds of $\sim 10^4$ - $10^5 M_\odot$ (Loeb & Rasio 1994; Koushiappas et al. 2004; Volonteri & Stark 2011; Bellovary et al. 2011), via stellar remnants from Pop III stars, resulting in low mass ($\sim 100 M_\odot$) black hole seeds (Madau & Rees 2001; Heger & Woosley 2002) or via a direct seed formation in a merger event as seen in the numerical simulations of Mayer et al. (2010). Second, another matter of vigorous debate is the process or processes that trigger and regulate accretion onto the central super-massive black hole. Mergers appear to be a physically well-motivated candidate (see e.g. Hopkins et al. 2006, 2008), but the observational situation still remains unclear in this respect: Some observational studies do find a statistically significant enhancement of merger signatures (as close pairs or a morphological disturbance) among (mainly high-luminosity) AGN host galaxies (e.g. Jogee et al. 2008; Ellison et al. 2011; Treister et al. 2012), but other observational works have repeatedly failed to find such an evidence for (mainly moderately) luminous AGN hosts up to $z \sim 2.5$ (Cisternas et al. 2010; Georgakakis et al. 2009; Pierce et al. 2007; Grogin et al. 2005; Li et al. 2008; Ellison et al. 2008; Schawinski et al. 2011; Kocevski et al. 2012).

To assess and clarify some of the above unresolved issues in a more self-consistent way than it can be achieved by e.g. semi-analytical or semi-empirical models, *large cosmological*, hydrodynamic simulations have been performed by several recent studies (Di Matteo et al. 2008; McCarthy et al. 2010; Degraf et al. 2010; McCarthy et al. 2011; Degraf et al. 2011; Booth & Schaye 2011; Di Matteo et al. 2012; DeGraf et al. 2012). Compared to semi-analytical models, they have the advantage that the dynamics of the baryonic component (gas and stars) and the interaction between baryonic matter can be followed directly in a cosmological context, even if the spatial and mass resolution, at present, is not high enough to accurately simulate small scale physical processes like e.g. the formation of stars and black holes with the associated feedback. Instead, they have to be computed in a simplified manner with sub-grid/sub-resolution models. Nevertheless, they provide a powerful tool to assess the cosmic evolution of statistical AGN and black hole properties and thus, go beyond the hydrodynamic isolated merger simulations. Di Matteo et al. (2008) and Booth & Schaye (2011), for example, investigated the global history of black hole mass assembly and the evolution of the black hole-bulge mass relations in cosmological simulations with a maximum box size of $\sim (50 \text{ Mpc})^3$. Such simulations have also been successful in reproducing the low-luminosity end of the AGN luminosity function (Degraf et al. 2010) or black hole clus-

tering properties (Degraf et al. 2011) but have been limited by a box size being not large enough to follow the evolution of luminous AGN with $L_{\text{bol}} \geq 10^{45} \text{ erg/s}$ (i.e. AGN luminosities above the exponential cut-off of the luminosity function). Most recently Di Matteo et al. (2012) and DeGraf et al. (2012) started to assess the growth of the first quasars appearing in the Universe by performing large simulations with a box size of $(500 \text{ Mpc/h})^3$, however, only run down to redshift $z = 5$. In their simulations, they find a rapid, early growth of black holes driven by cold, infalling gas flows being consistent with the existence of $\sim 10^9 M_\odot$ black holes as early as $z \sim 7$. At these early times, quasar feedback is found to be not effective at stopping the cold gas from penetrating the central regions and hence cannot quench the accretion until the host galaxy reaches $M_{\text{halo}} \gtrsim 10^{12} M_\odot$. In addition, major galaxy mergers are not required for an efficient fuel supply and growth.

In contrast, in this work, we extend their studies of the cosmic evolution of statistical properties of black hole growth and AGN evolution at *lower* redshifts, from $z \sim 5$ down to $z = 0$. We analyse a subset of cosmological, hydrodynamical simulations from the *Magneticum Pathfinder* simulation set (Dolag et al., in prep), which includes a large cosmological box with $(180 \text{ Mpc})^3$. The simulations include a self-consistent model for black hole growth using the Gadget3 code containing several modifications for modelling the growth of black holes compared to previous studies (e.g. Di Matteo et al. 2008, 2012). We will particularly focus on the evolution of the AGN luminosity function and the connected anti-hierarchical/downsizing trend in AGN number densities with the aim to understand its origin within a hierarchical structure formation scenario. In this context, we test the effect of empirically motivated dust obscuration models and discuss implications of the downsizing trend on the interplay between AGN luminosities, black hole mass and Eddington-ratios. Overall, in this study, we go beyond previous papers of e.g. Di Matteo et al. (2008) or Degraf et al. (2010) as we examine the evolution of the AGN luminosity function in a by a factor of ~ 15 larger cosmological volume with comparably good resolution allowing us to probe also luminous AGN with $L_{\text{bol}} \geq 10^{45} \text{ erg/s}$.

This study is organised as follows. Section 2 gives an overview of the simulation code and the corresponding model for black hole growth and AGN feedback adopted in our simulations. In Section 3 we present some basic properties of present-day and high-redshift black holes and galaxies, which are compared to observational data. We study the evolution of the AGN luminosity function in Section 4 for low redshifts ($z < 3$) and in Section 5 for high redshifts ($3 < z < 5$), considering bolometric, soft and hard X-ray and (for $z = 0$ only) also radio luminosities, and compare our results to observational data. In Section 6, we explicitly show the evolution of the AGN number density and discuss the anti-hierarchical trend in black hole growth, its consequences on the connection between black hole masses and AGN luminosities and its numerical origin in our simulations. In the end, in Section 7, we summarise and discuss our main results.

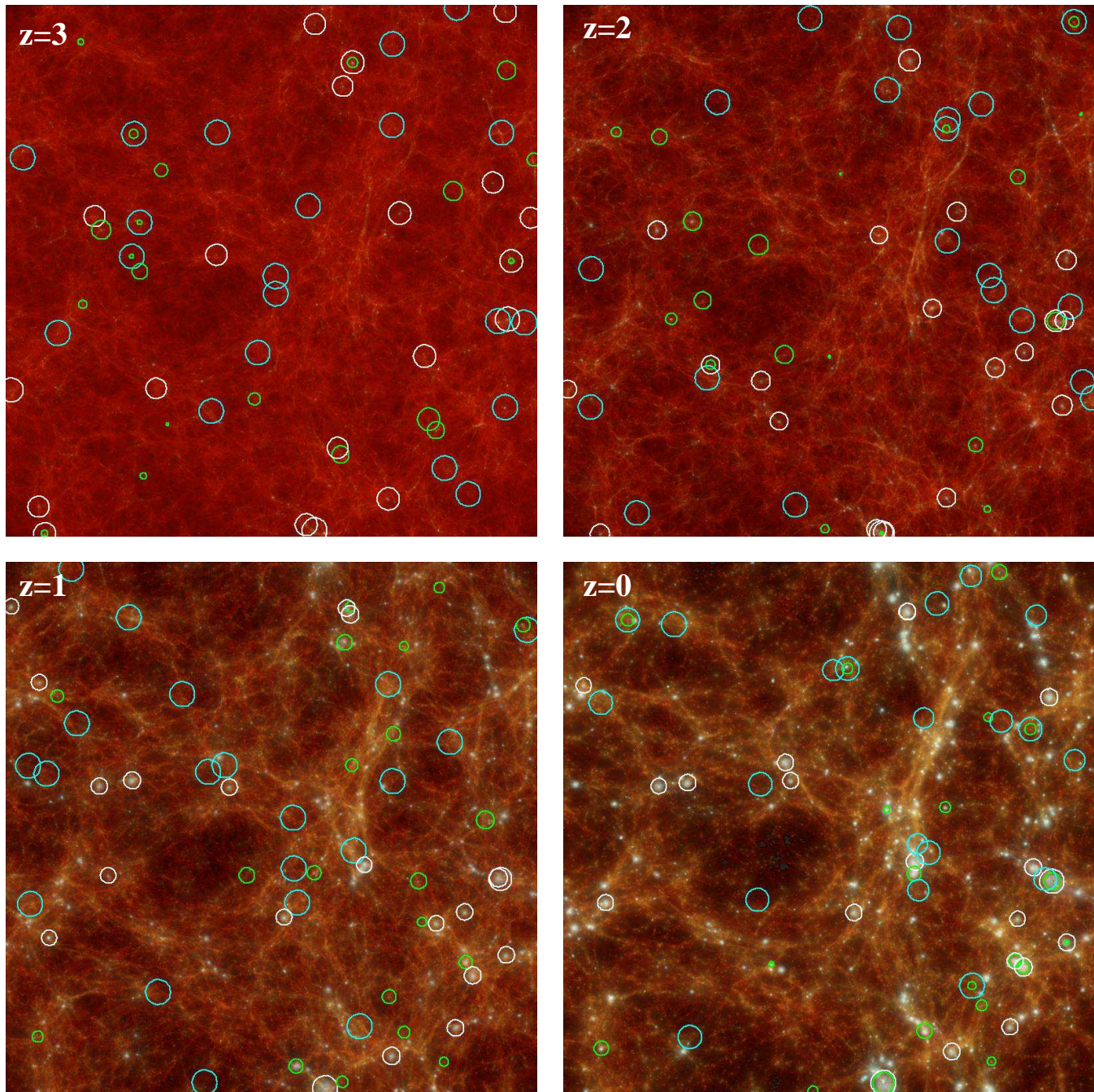


Figure 1. The cosmological baryonic mass distribution (stellar and gaseous density) of the Box3/hr simulation at different redshift steps ($z=3,2,1$ and 0). White, cyan and green circles indicate the 20 black holes with the highest masses, the highest Eddington-ratios and the highest accretion rates, i.e. AGN luminosities, respectively. The sizes of the circles are scaled logarithmically with the different values, normalised to maximum value of each quantity.

2 THE SIMULATIONS

In this paper, we analyse a subset of cosmological boxes from the Magneticum Pathfinder simulation set (Dolag et al., in prep.). From this set, we selected a medium size cosmological simulation with a co-moving box size of $(128\text{Mpc}/h)^3$, simulated with an initial particle number of 2×576^3 (Box3-hr, which is our “large” run throughout this study) and one cosmological simulation with a smaller co-moving box size of $(48\text{Mpc}/h)^3$, sampled with the same particle number and

therefore, an increased resolution (Box4-uhr). Table 1 gives an overview of the two simulation runs. We have adopted a Λ CDM model with parameters chosen according to the seven-year *Wilkinson Microwave Anisotropy Probe* WMAP7 data (Komatsu et al. 2011) with $\Omega_m = 0.272$, $\Omega_b = 0.0456$, $\Omega_\Lambda = 0.728$ and $h = 0.704$. The initial power spectrum follows $n = 0.963$ and is normalised to $\sigma_8 = 0.809$.

Table 1. Overview of the two simulation runs which are analysed in this study.

Name	Box size [Mpc/h]	Resolution level	Initial particle number	m(dm) [M_\odot]	m(gas) [M_\odot]	m(stars) [M_\odot]	Softening length [kpc/h]
Box3	128	hr	2×576^3	6.9×10^8	1.4×10^8	3.5×10^7	3.75
Box4	48	uhr	2×576^3	3.6×10^7	7.3×10^6	1.8×10^5	1.4

2.1 The numerical code

Our simulations are based on the parallel cosmological TreePM-SPH code P-GADGET3 (Springel 2005). The code uses an entropy-conserving formulation of SPH (Springel & Hernquist 2002) and follows the gas using a low-viscosity SPH scheme to properly track turbulence (Dolag et al. 2005). It also allows a treatment of radiative cooling, heating from a uniform time-dependent ultraviolet background and star formation with the associated feedback processes. The latter is based on a sub-resolution model for the multiphase structure of the interstellar medium (Springel & Hernquist 2003).

Radiative cooling rates are computed by following the same procedure presented by Wiersma et al. (2009). We account for the presence of the cosmic microwave background (CMB) and of ultraviolet (UV)/X-ray background radiation from quasars and galaxies, as computed by Haardt & Madau (2001). The contributions to cooling from each one of 11 elements (H, He, C, N, O, Ne, Mg, Si, S, Ca, Fe) have been pre-computed using the publicly available CLOUDY photo-ionisation code (Ferland et al. 1998) for an optically thin gas in (photo-)ionisation equilibrium.

In the multiphase model for star-formation (Springel & Hernquist 2003), the ISM is treated as a two-phase medium where clouds of cold gas form from cooling of hot gas and are embedded in the hot gas phase assuming pressure equilibrium whenever gas particles are above a given threshold density. The hot gas within the multiphase model is heated by supernovae and can evaporate the cold clouds. A certain fraction of massive stars (10 per cent) is assumed to explode as supernovae type II (SNII). The released energy by SNII (10^{51} erg) is modelled to trigger galactic winds with a mass loading rate being proportional to the star formation rate (SFR) to obtain a resulting wind velocity of $v_{\text{wind}} = 350$ km/s. Our simulations also include a detailed model of chemical evolution according to Tornatore et al. (2007). Metals are produced by SNII, by supernovae type Ia (SNIa) and by intermediate and low-mass stars in the asymptotic giant branch (AGB). Metals and energy are released by stars of different mass to properly account for mass-dependent life-times (with a lifetime function according to Padovani & Matteucci 1993), the metallicity-dependent stellar yields by Woosley & Weaver (1995) for SNII, the yields by van den Hoek & Groenewegen (1997) for AGB stars and the yields by Thielemann et al. (2003) for SNIa. Stars of different mass are initially distributed according to a Chabrier initial mass function (IMF; Chabrier 2003).

2.2 The black hole growth model

Most importantly, our simulations also include a prescription for black hole growth and for a feedback from active galactic nuclei (AGN) based on the model presented in Springel et al. (2005b) and Di Matteo et al. (2005) including the same modifications as in the study of Fabjan et al. (2010) and some new, minor changes.

As for star formation, the accretion onto black holes and the associated feedback adopts a sub-resolution model. Black holes are represented by collision-less “sink particles” that can grow in mass by accreting gas from their environments, or by merging with other black holes.

The gas accretion rate \dot{M}_\bullet is estimated by using the Bondi-Hoyle-Lyttleton approximation (Hoyle & Lyttleton 1939; Bondi & Hoyle 1944; Bondi 1952):

$$\dot{M}_\bullet = \frac{4\pi G^2 M_\bullet^2 \alpha \rho}{(c_s^2 + v^2)^{3/2}}, \quad (1)$$

where ρ and c_s are the density and the sound speed of the surrounding (ISM) gas, respectively, v is the velocity of the black hole relative to the surrounding gas and α is a boost factor for the density which typically is set to 100 as in most related works (unless a more detailed description as introduced in Booth & Schaye (2009) is used) and accounts for the fact that in cosmological simulations we can not resolve the intra-cluster medium (ICM) properties within the vicinity of the black hole. The black hole accretion is always limited to the Eddington rate (maximum possible accretion for balance between inwards directed gravitational force and outwards directed radiation pressure): $\dot{M}_\bullet = \min(\dot{M}_\bullet, \dot{M}_{\text{edd}})$. Note that the detailed accretion flows onto the black holes are unresolved, we can only capture black hole growth due to the larger scale gas distribution, which is resolved. Once the accretion rate is computed for each black hole particle the mass continuously grows. To model the loss of this accreted gas from the gas particles, a stochastic criterion is used to select the surrounding gas particles to be accreted. Unlike in Springel et al. (2005b), in which a selected gas particle contributes to accretion with all its mass, we include the possibility for a gas particle to accrete only with a slice of its mass, which corresponds to 1/4 of its original mass. In this way, each gas particle can contribute with up to four generations of black hole accretion events, thus providing a more continuous description of the accretion process.

The radiated luminosity L_{rad} is related to the black hole accretion rate by

$$L_{\text{rad}} = \frac{\epsilon_r}{1 - \epsilon_r} \dot{M}_\bullet c^2, \quad (2)$$

where ϵ_r is the radiative efficiency, for which we adopt a fixed

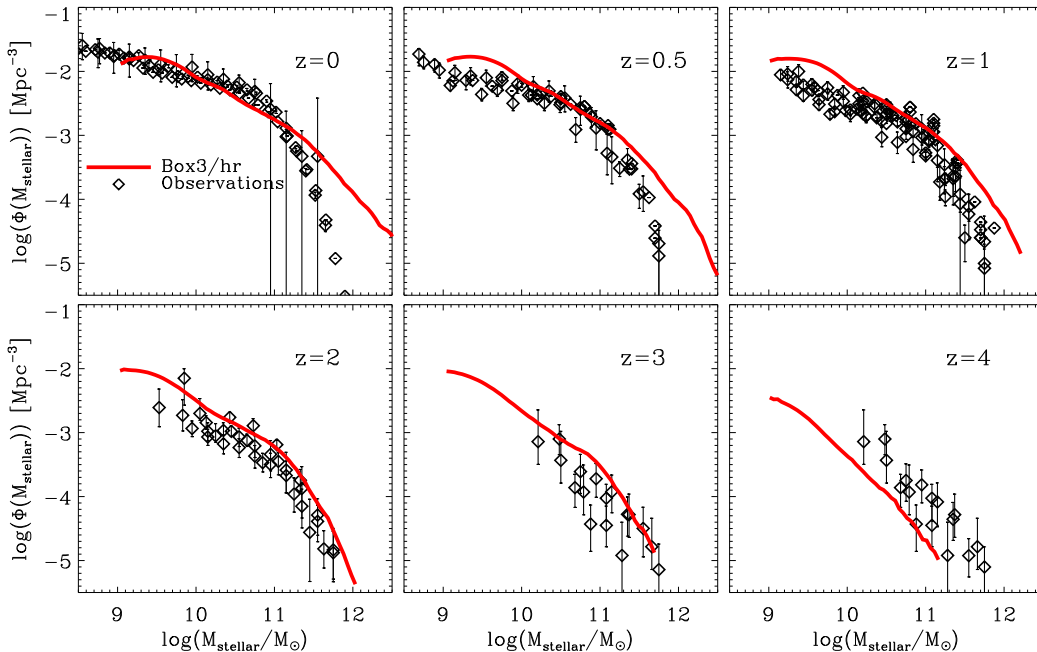


Figure 2. Evolution of the stellar mass function in the Box3-hr simulation (red lines) compared to observational data (black symbols, Pérez-González et al. 2008; Bundy et al. 2005; Drory et al. 2004; Fontana et al. 2006; Marchesini et al. 2007; Ilbert et al. 2010). At $z < 1$ the massive end is over-estimated in the simulations due to a too inefficiently working radio-mode feedback.

value of 0.1 (standardly assumed for a radiatively efficient accretion disk onto a non-rapidly spinning black hole according to Shakura & Sunyaev 1973, see also Springel 2005; Di Matteo et al. 2005). We assume that a fraction ϵ_f of the radiated energy is thermally coupled to the surrounding gas so that $\dot{E}_f = \frac{\epsilon_f}{1-\epsilon_f} \epsilon_f \dot{M}_\bullet c^2$ is the rate of the energy feedback. ϵ_f is a free parameter and typically set to 0.1. The energy is distributed kernel weighted to the surrounding gas particles in an SPH like manner. Additional, we incorporated the feedback prescription according to Fabjan et al. (2010): we account for a transition from a quasar- to a radio-mode feedback (see also Sijacki et al. 2007) whenever the accretion rate falls below an Eddington-ratio of $f_{\text{edd}} := \dot{M}_r / \dot{M}_{\text{edd}} < 10^{-2}$. During the radio-mode feedback we assume a 4 times larger feedback efficiency than in the quasar mode. This way, we want to account for massive black holes, which are radiatively inefficient (having low accretion rates), but which are efficient in heating the ICM by inflating hot bubbles in correspondence of the termination of AGN jets. Note that we also, in contrast to Springel et al. (2005b), modify the mass growth of the black hole by taking into account the feedback, e.g. $\Delta M_\bullet = (1 - \epsilon_r) M_\bullet \Delta t$. Additionally, we introduced some technical modifications of the original implementation:

(I) One difference with respect to the original implementation by Springel et al. (2005b) concerns the seeding of black hole particles. In the implementation by Springel et al. (2005b), black hole particles are seeded in a halo whenever it first reaches a minimum (total) friends-of-friends (FoF) halo mass, where the FoF is performed on the dark matter particles only. In order to guarantee that black holes are seeded only in halos where sufficient star formation took place, our implementation performs a FoF algorithm on star particles,

grouping them with a linking length of about 0.05 times the mean separation of the DM particles¹. In the simulations presented here, a total stellar mass of $10^{10} M_\odot/h$ is needed for a halo to be seeded with a black hole particle (starting with a seed mass of $2 \times 10^9 M_\odot/h$). Furthermore, we locate seeded black holes at the potential minimum of the FoF group, instead of at the density maximum, as originally implemented.

(II) In the original implementation by Springel et al. (2005b), black holes are forced to remain within the host galaxy by pinning them to the position of the particle found having the minimum value of the potential among all the particles lying within the SPH smoothing length compute at the black hole position. Within a cosmological context an aside effect of this criterion is that, due to the relatively large values of SPH smoothing lengths, a black hole can be removed from the host galaxy whenever it becomes a satellite, and is spuriously merged into the black hole hosted in the central halo galaxy. We have relaxed this criterion and do not apply any pinning of the black hole particles to the minimum potential within the smoothing length. To avoid that the black hole particles are wandering away from the centre of galaxies by numerical effects, we take several measures, in addition to the original implementation of the black hole treatment: first we enforce a more strict momentum conservation within the implementation of gas accretion by forcing momentum conservation for the smooth accretion of the gas and then do not model any momentum transfer when swal-

¹ Note that this linking length is thus much smaller than that, 0.150.20, originally used, to identify virialised halos.

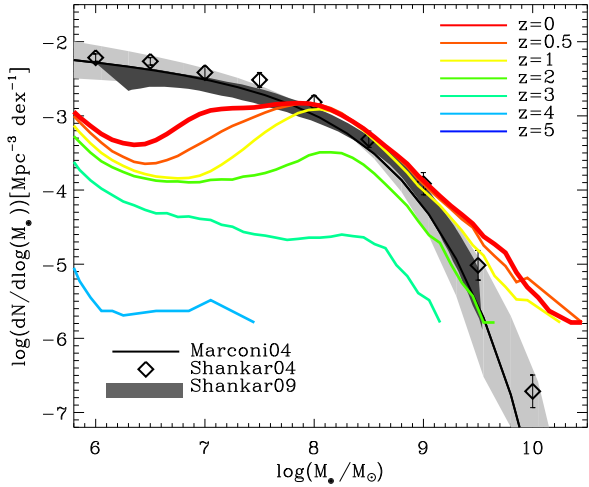


Figure 3. Evolution of the black hole mass function in the Box3-hr simulation (coloured lines). The present-day black hole mass function (red line) is compared to observations from Marconi et al. (2004); Shankar et al. (2004) and Shankar et al. (2009) (black lines and symbols with the grey shaded areas). We find a reasonable agreement between observations and simulations for black hole masses above $10^8 M_\odot$ with an over-estimation of the most massive black holes by roughly ~ 0.5 dex. This results from the fact that we over-estimate the number of massive galaxies.

lowing gas². Additionally we implemented the conservation of momentum and centre of mass when two black hole particles are merging.

Moreover, in contrast to the original implementation, we have included explicitly a dynamical friction force, which in cosmological simulations is typically numerically not resolved. To estimate the typical friction force induced onto a black hole particle we are using the following approximation of the Chandrasekhar formula (Chandrasekhar 1943):

$$F_{\text{df}} = -4\pi \left(\frac{GM_\bullet}{v} \right)^2 \rho \ln(\Lambda) \left(\text{erf}(x) - \frac{2x}{\sqrt{\pi}} e^{-x^2} \right) \frac{\vec{v}}{v},$$

where G is the gravitational constant and M_\bullet is the mass of the black hole. The local density ρ in the vicinity of the black hole as well as for the relative velocity \vec{v} is calculated using only the stellar and the dark matter components around the black hole. The Coulomb logarithm is calculated as

$$\ln(\Lambda) = \ln \left(\frac{Rv}{GM_\bullet} \right)$$

and $x = v\sqrt{2}/\sigma$, where we estimate σ as one third of the maximum circular velocity of the hosting sub-halo and for R (as typical size of the system) we used the half mass radius of the sub-halo, hosting the black hole. The parameters of the hosting sub-halo for each black hole particle are updated every time when SubFind is executed on-the-fly.

In this way a black hole particle remains within the host galaxy, even when it becomes a satellite of a larger halo and compared to the original scheme we are able to track

² Note that otherwise one would statistically account for the momentum transfer of accreted gas twice.

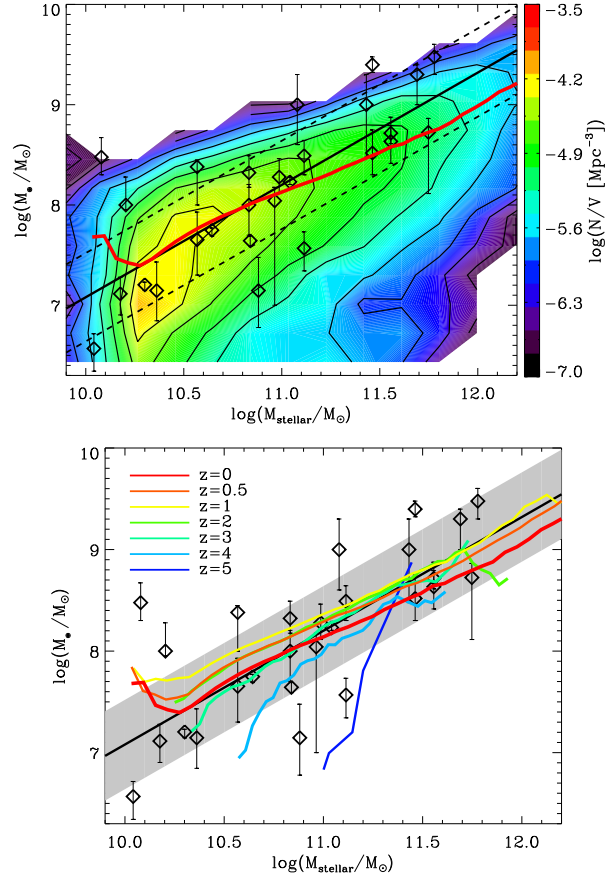


Figure 4. *Upper panel:* present-day relation between black hole and stellar mass. Colour-coded contours show the simulated number density, the red line illustrates the mean for the Box3-hr run. This is compared to observations of Häring & Rix (2004) (symbols illustrate their data set, the black solid line the fit to the data and the black dashed lines the corresponding $1-\sigma$ scatter). Simulations match the observed relation reasonably well within the $1-\sigma$ scatter. *Bottom panel:* Evolution of the black hole-stellar mass relation in the Box3-hr run (coloured lines). For comparison, the observational data of the present-day relation is also illustrated as in the upper panel. In the simulation, the black hole-bulge mass relation is in place at $z = 3$ and hardly evolves afterwards.

black holes also in satellite galaxies in cluster environments. When the black holes are not placed artificially on the minimum of the potential, of course, there is no guarantee (due to numerical noise and 2 body scattering) that black hole particles are staying always exactly at the local potential minimum. But due to all the improvements in handling the black hole component as described before, typical displacements of the true potential minimum are of the order of the effective gravitational softening and therefore order of magnitudes smaller than the typical smoothing radius used for estimating the parameters in the accretion model or used for distributing the feedback energy. They, therefore, do not play any significant role for the behaviour of the model.

Fig. 1 shows a visualisation (of the gas and stellar mass density) of the Box3-hr run at different redshift steps ($z = 3 - 0$, different panels). Additionally, we have indicated the 20 black holes with highest masses (white circles), the

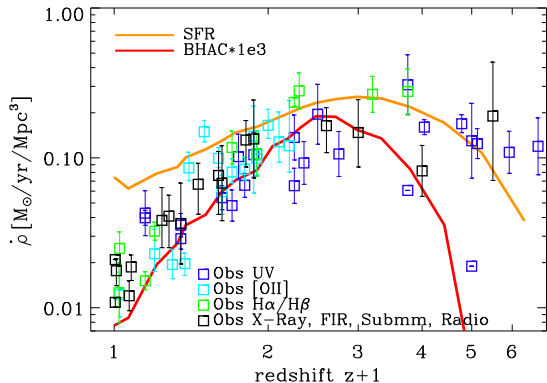


Figure 5. Cosmic evolution of mean star formation (orange line) and black hole accretion rate densities multiplied by a factor of 10^3 (red line) in the Box3-hr run. Both, star formation and black hole accretion rate densities peak between $z = 1 - 2$ followed by a decline towards lower redshifts. Simulations are compared to observed cosmic star formation rate densities derived from different wavebands (coloured symbols, Hopkins & Beacom 2006), and they predict too high star formation rates at $z < 1$ as a consequence of a too inefficient radio-mode feedback (see also Fig. 2).

highest Eddington-ratios ($f_{\text{edd}} = L/L_{\text{edd}}$, green circles) and the highest accretion rates (and thus, luminosities, cyan circles). The sizes of the circles are scaled logarithmically with the different values and normalised to the maximum value of each quantity. It visualises that AGN luminosity does not directly trace the mass of a black hole as AGN when selected by their black hole mass (white) seem to be a better tracer of the underlying matter distribution, whereas when selected by the Eddington-ratio (green) or by their luminosity (cyan) they are more located in less dense environments, what already indicates the presence of a “downsizing” trend in their evolution.

3 FUNDAMENTAL GALAXY AND BLACK HOLE PROPERTIES AND THEIR EVOLUTION

In this section, we will discuss some fundamental properties of the simulated galaxies and black holes in the Box3-hr run, the stellar mass function, the black hole mass function and the black hole-stellar mass relation in the present-day Universe and at higher redshifts. Note that using the Box4-ubr simulation hardly changes any of these results (and is, thus, not shown explicitly).

Fig. 2 shows the stellar mass function at different redshift steps as indicated in the legend. Simulation results (red lines) are compared with observational data from different studies (black symbols, Pérez-González et al. 2008; Bundy et al. 2005; Drory et al. 2004; Fontana et al. 2006; Marchesini et al. 2007; Ilbert et al. 2010). At $z = 4$, the amount of galaxies is slightly under-estimated, what is, however, a resolution effect: for the Box4-ubr simulation the low-mass end of the stellar mass function at these high redshifts is not under-estimated. Instead, down to $z = 1$

the simulation results provide a good match with the observational data. However, turning towards even lower redshifts ($z < 1$), the massive end of the stellar mass function ($M_{\text{stellar}} > 10^{11} M_{\odot}$) is significantly over-estimated in the simulation, e.g. at $z = 0$ by more than one order of magnitude for $10^{12} M_{\odot}$ -mass galaxies. This is most likely a consequence of a too inefficiently working “radio-mode” feedback. Here we may speculate that a mechanical-momentum input from an AGN coupling to the ambient gas via a bipolar wind would be more efficient in limiting the infall and accretion onto the central BH and also star formation and thus, could help making elliptical galaxies red and dead by suppressing late star formation. This is for example suggested by simulations of isolated galaxies or galaxy mergers (Choi et al. 2012; Debuhr et al. 2012; Barai et al. 2013).

In Fig. 3, the present-day black hole mass function in our simulation (red line) is shown and compared to observations from Marconi et al. (2004); Shankar et al. (2004) and Shankar et al. (2009) (black lines and symbols and grey shaded areas). We find a reasonably good agreement between simulations and observations for a black hole mass range of $7.5 < \log(M_{\bullet}/M_{\odot}) < 9.5$. Below, simulations are under-predicting the amount of low massive black holes by almost one order of magnitude. This is mainly related to a combination of too low resolution (main effect) and black hole seed masses. Turning to the high mass end, the amount of massive black holes $\log(M_{\bullet}/M_{\odot}) > 9.5$ is over-estimated by roughly 0.5 dex. The high mass end is mostly influenced by the choice for the parameter regulating the strength for AGN feedback, but hardly dependent on the efficiency parameter for regulating the Radio-mode feedback. Although the later is regulating the late time star formation and black hole growth, in the implementation we are using this is still not efficient enough for the high mass end of stellar and black hole mass functions. Therefore, AGN feedback at high redshift is much more efficient in suppressing star formation also at late time by pre-heating the environment. Turning towards higher redshifts (see coloured lines in Fig. 3), one can see a very rapid evolution until $z = 1$, where the high mass end is already in place and only the amount of black holes below $\log(M_{\bullet}/M_{\odot}) < 8$ still increases until $z = 0$. This implies that black holes grow most strongly until $z = 1$ what is also in agreement when looking at the cosmic evolution of the total black hole accretion rates, which peak around $z = 2$ and fall below $0.1 M_{\odot} \text{ yr}^{-1} \text{ Mpc}^{-3}$ after $z = 1$ (see also Fig. 5).

The top panel of Fig. 4 illustrates another fundamental property of black holes, namely a colour-coded 2-dimensional histogram of the black hole-stellar mass relation in the present-day Universe, the mean relation is indicated by the red line. For simplicity, we have used the whole stellar mass and not only the bulge mass, which is normally considered in observations. However, galaxies with masses above $\log(M_{\text{stellar}}/M_{\odot}) > 10.5$ are largely systems consisting of a spherical component in our simulations as their resolution is not high enough to provide sufficient morphological information of the galaxies. Compared to observations from Häring & Rix (2004) (black lines and symbols), we find an overall good agreement with the simulations within the observed $1-\sigma$ scatter (black dashed lines). However, on average, for stellar masses above $\log(M_{\text{stellar}}/M_{\odot}) > 11$, the black holes in the simulations tend to be slightly under-massive

for a given stellar mass, although simulations predict too many massive black holes as we have seen in Fig. 3. This mismatch is due to the fact that simulations also significantly over-estimate massive galaxies at low redshift most likely as a consequence of the too inefficient radio-mode feedback (see Fig. 2). As a consequence, the black hole-to-stellar mass ratio is significantly lowered.

Turning to the evolution of the black hole-stellar mass relation (coloured lines in the bottom panel of Fig. 4), the relation is in place at $z = 3$ (see turquoise line). Below $z = 3$, the slope of the relation is much steeper than the one of the present-day relation and the black hole masses are mainly found to be under-massive for a given stellar mass. However, this is just due to resolution: for the Box4-*uhr*, the relation is already in place at $z = 5$, as particularly the accretion of small black holes is much better resolved. Note that the interplay between stellar and BH mass on one side, and cooling, feedback efficiency for star-formation and AGN treatment on the other side is quite complex. So although most overall properties seems to behave well when changing resolution, some of the details might need adaption of the parameters of the underlying models when going to higher and higher resolution. Between $z = 1$ and $z = 3$, the black hole-to-stellar mass ratio is slightly increasing for a given stellar mass, i.e. black holes are growing somewhat stronger than the corresponding galaxy stellar masses. In contrast, afterwards ($z < 1$), this ratio decreases until today, i.e. the relation is just shifted towards more massive galaxy masses, what is most likely due to the strong late growth of massive galaxies. Overall, this is mainly consistent with previous results from cosmological simulation (Di Matteo et al. 2008).

Observationally, star formation and black hole accretion rate densities ($\dot{\rho}_{\text{stellar}}$ and $\dot{\rho}_{\bullet}$, respectively) are found to trace each other over cosmic time with $\dot{\rho}_{\text{stellar}} \sim 10^3 \times \dot{\rho}_{\bullet}$ (e.g. Zheng et al. 2009 and references therein). Therefore, in Fig. 5 we present the cosmic evolution of the star formation rate and black hole accretion rate densities multiplied with a factor of 10^3 in our Box3-*hr* run (orange and red lines, respectively). They are compared to an observational compilation of Hopkins & Beacom (2006) for the star formation rate densities derived from different wavebands (differently coloured symbols). At high redshifts, simulated black hole accretion rate densities are slightly too low compared to the simulated and observed star formation rate densities, which is most likely again a consequence of resolution and black hole seeding. Both, simulated star formation and black hole accretion rates peak between $z = 1 - 2$, in agreement with observations, followed by a decline towards lower redshifts. While the black hole accretion rate densities are, however, in reasonable agreement with the observed data (for the star formation rates), the simulated star formation rates are too high (e.g. by a factor of 3-4 at $z = 0$) – a consequence of too inefficient radio-mode feedback and thus, resulting in too massive present-day galaxies, as we have discussed earlier in Fig. 2.

4 THE AGN LUMINOSITY FUNCTION UP TO $Z=2.5$

In this section, we focus on both radiatively efficient and inefficient AGN in the Box3-*hr* run (note that the results for

moderately luminous AGN hardly change for the Box4-*uhr* run) by comparing their radiative bolometric at low redshifts $z < 2.5$ as well as their present-day radio luminosities to observational data. For an improved comparison with observations, we also derive the soft and hard X-ray luminosities and adopt a dust obscuration model (on a torus level) being dependent on both redshift and AGN luminosity.

4.1 Bolometric luminosities

The bolometric luminosity L_{bol} (=radiative luminosity) is calculated according to Eq. 2. Fig. 6 shows the bolometric luminosity function at different redshift steps (different panels). Our simulation results spanning a broad luminosity range of $10^{42.5} \text{ erg s}^{-1} < L_{\text{bol}} < 10^{48} \text{ erg s}^{-1}$ (red solid lines) are compared to the observational compilation from Hopkins et al. (2007) (black symbols). In this study, they convert the AGN luminosities from different observational data sets and thus, from different wavebands (emission lines, NIR, optical, soft and hard X-ray) into bolometric ones. Overall, for the shown redshift range, we obtain a reasonably good agreement between simulations and observations. Only at $z < 1$, the amount of the highest luminous AGN ($L_{\text{bol}} \geq 10^{47} \text{ erg s}^{-1}$) is slightly over-estimated by up to 0.5 dex. Such high luminosities can only occur for black holes more massive than $10^9 M_{\odot}$. Therefore, this mismatch is most likely related to the fact that the simulations predict too many very massive black holes (with masses above $3 \times 10^9 M_{\odot}$) at low redshift probably as a consequence of a slightly too small AGN feedback efficiency parameter (see red line in Fig. 3).

Nevertheless, the overall good agreement between simulations and observations may indicate that the black hole growth closely follows the gas density and other physical quantities included in the Bondi-Hoyle accretion formula equation 1 in the resolved vicinity of the black hole although simulations are not able to capture the physical processes on small scales, i.e. do not resolve the inner parts of the black hole (3.75 kpc/h) and thus, adopt a very rough approximation for the accretion process itself. Still, simulations seem at least to be able to capture the right trends of how black holes grow (we will discuss this in more detail in section 6.3). We want to point out that going to our higher resolution simulation Box4-*uhr* (combined with a lower box size), the low luminosity end is still in agreement with observations showing that the simulation results converge going to higher resolution (see also section 5). A previous study of Degraf et al. (2010) has also investigated the evolution of the AGN luminosity function in cosmological simulations with similar and larger resolution to ours. However, their simulations have a significantly smaller box-size so that they can only probe the low-luminosity end of the AGN luminosity function (up to $L_{\text{bol}} < 10^{45} \text{ erg s}^{-1}$), which they find to be in reasonably good agreement with observations. Due to their small box-size, they cannot investigate the evolution above the exponential cut-off of the AGN luminosity function as it is shown *for the first time* for our large, cosmological simulation Box3-*hr*.

In the study of Hopkins et al. (2007), which we have our simulation predictions compared to in Fig. 6, they only assume a *luminosity* dependence of the obscured fraction (the less luminous the more obscured) and the same num-

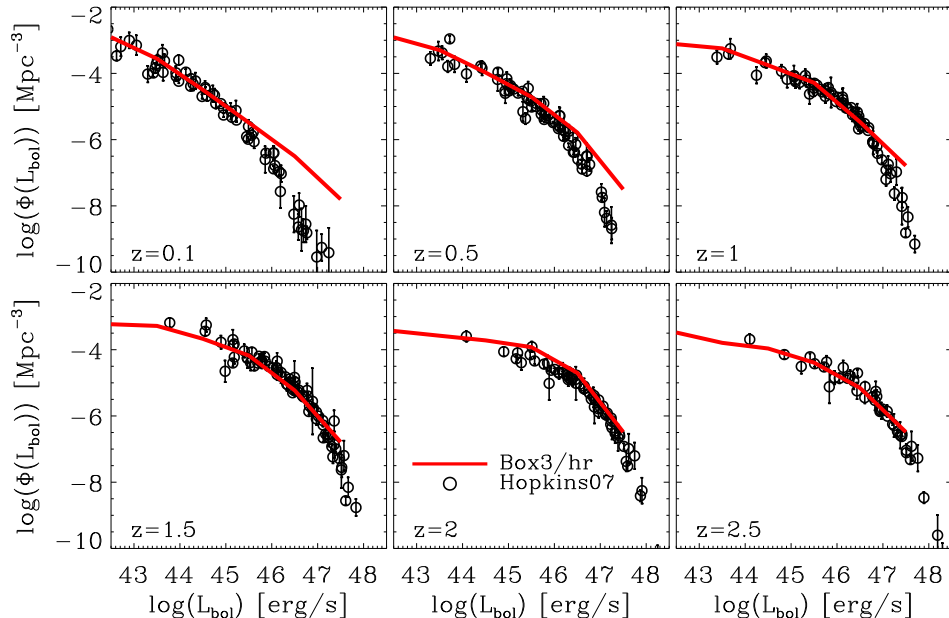


Figure 6. Evolution of the bolometric AGN luminosity function for the Box3-hr simulation (red solid lines) at $z = 0 - 2.5$. Simulation predictions match the observational data of Hopkins et al. (2007) (black, open circles) fairly well.

ber of Compton-thick ($N_H > 10^{24} \text{ cm}^{-2}$) and Compton-thin ($10^{23} \text{ cm}^{-2} < N_H < 10^{24} \text{ cm}^{-2}$) AGN. But there are many aspects of the obscuration corrections that are still being vigorously debated. Some recent studies suggest that the obscured fraction is dependent on both luminosity and redshift (Hasinger 2008; Fiore et al. 2012), in contrast with the non-redshift dependent model of Hopkins et al. (2007). There are also uncertainties with respect to the dust correction for the UV luminosity; Hopkins et al. (2007) compute the amount of dust (and therefore extinction), by adopting an N_H distribution from X-ray observations, and a Galactic dust-to-gas ratio. However, it has been shown that AGN absorbers do not have a Galactic dust to gas ratio (Maiolino et al. 2001, 2004). The result is that they probably over-estimate the extinction, which might result in slightly higher luminosities for the optically selected quasars (F. Fiore, personal communication). Because of these uncertainties, we additionally attempt in subsection 4.2 to correct our model predictions for obscuration and to directly compare them with recent soft and hard X-ray measurements of the AGN luminosity function.

4.2 X-ray luminosities

We now compare our simulation predictions with recent observational determinations of the AGN luminosity function in the hard (2 – 10 keV) and soft (0.5 – 2 keV) X-ray bands (Hasinger et al. 2005; Ebrero et al. 2009; Aird et al. 2010; Fiore et al. 2012). In contrast to the previous section, we do not attempt to correct the observations for obscuration, but instead apply an obscuration correction to our models. We convert the modelled, bolometric luminosities into hard and soft X-ray luminosities (0.5 – 2 keV and > 2 keV) using the bolometric correction according to Marconi et al. (2004). In their study, the hard and soft X-ray luminosities L_{HXR} , L_{SXR}

are approximated by the following third-degree polynomial fits:

$$\log(L_{\text{HXR}}/L_{\text{bol}}) = -1.54 - 0.24\mathcal{L} - 0.012\mathcal{L}^2 + 0.0015\mathcal{L}^3 \quad (3)$$

$$\log(L_{\text{SXR}}/L_{\text{bol}}) = -1.65 - 0.22\mathcal{L} - 0.012\mathcal{L}^2 + 0.0015\mathcal{L}^3 \quad (4)$$

with $\mathcal{L} = \log(L_{\text{bol}}/L_{\odot}) - 12$. These corrections are derived from template spectra, which are truncated at $\lambda > 1 \mu\text{m}$ in order to remove the IR bump and which are assumed to be independent of redshift (therefore the resulting bolometric corrections are also assumed to be redshift independent). Additionally, we apply a correction for obscuration to the model luminosities, as suggested by several observational studies (Ueda et al. 2003; Hasinger 2004; La Franca et al. 2005), in which it has been shown that the fraction of obscured AGN is luminosity dependent and decreases with increasing luminosity. While older studies such as Ueda et al. (2003) and Steffen et al. (2003) did not find a clear dependence of obscuration on redshift, several recent observational studies (Ballantyne et al. 2006; Gilli et al. 2007; Hasinger 2008) propose a strong evolution of the obscured AGN population (with the relative fraction of obscured AGN increasing with increasing redshift). Here, we follow the study of Hasinger (2008), where they compare the same AGN in both the soft and hard X-ray band so that they can derive an approximation for the obscured fraction f_{obsc} in the soft X-ray band. The obscured fraction at $z < 2$ is then given by this equation:

$$f_{\text{obsc}}(z, L_{\text{SXR}}) = -0.281(\log(L_{\text{SXR}}) - 43.5) + 0.279(1 + z)^{\alpha}, \quad (5)$$

where L_{SXR} is the soft X-ray luminosity and they find that a value of $\alpha = 0.62$ provides the best fit to their observational data. The obscured fraction at $z > 2$ is approximately the

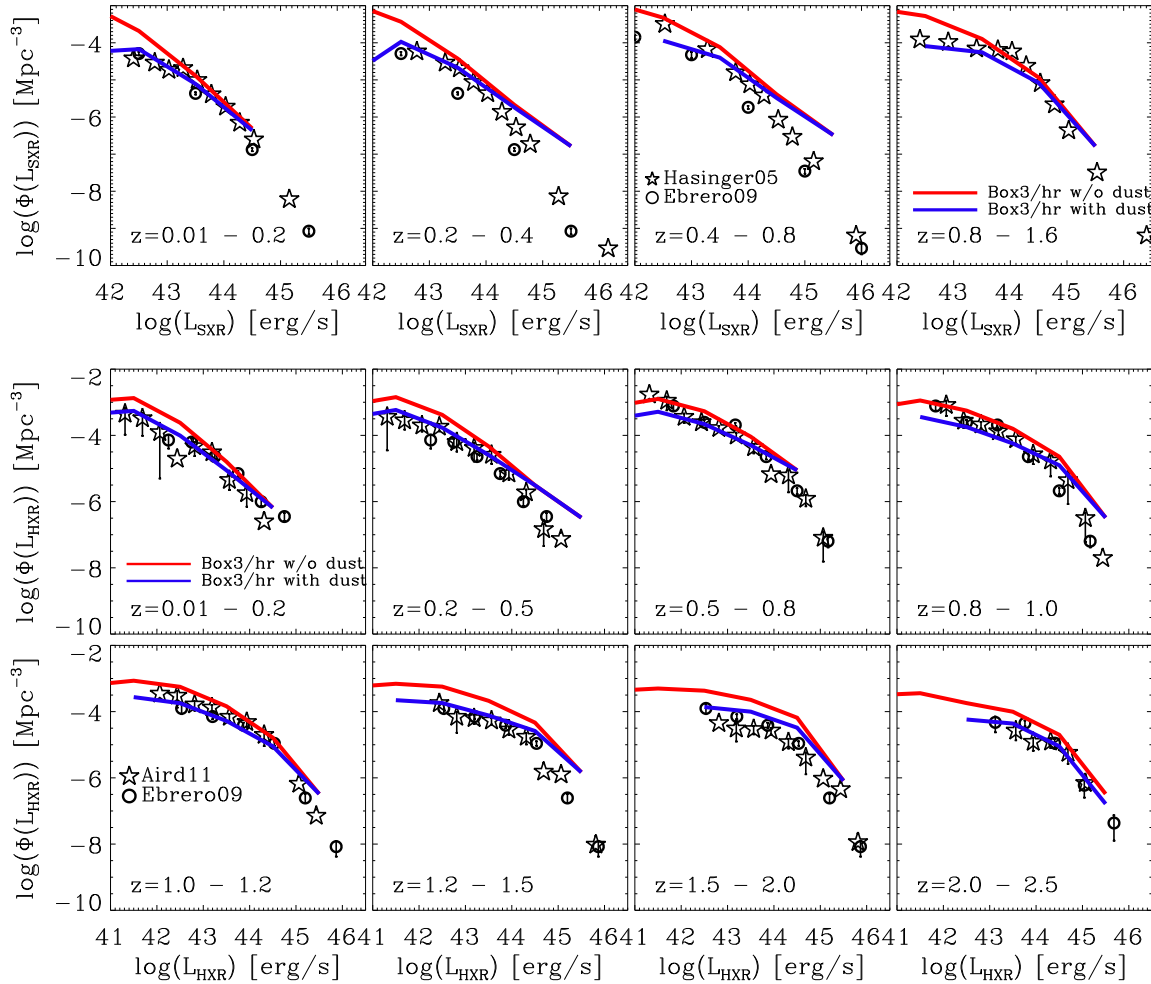


Figure 7. Top row: Evolution of the soft X-ray (0.5 – 2 keV) AGN luminosity function at $z = 0 - 1.6$. Middle and bottom rows: Evolution of the hard X-ray (2 – 10 keV) AGN luminosity function at $z = 0 - 2.5$. Blue and red solid lines always illustrate the results of the Box3-hr run with and without accounting for dust obscuration, respectively. For soft and hard X-ray luminosities at $z = 0 - 1.6$ and at $z = 1 - 2.5$, respectively, we find a better match with observational data (black symbols, Hasinger et al. 2005; Ebrero et al. 2009; Aird et al. 2010) when considering dust obscuration.

same at $z = 2$:

$$f_{\text{obs}}(z, L_{\text{SXR}}) = -0.281(\log(L_{\text{SXR}}) - 43.5) + 0.551. \quad (6)$$

Note that according to equations 5 and 6, the obscured fractions can get negative or larger than 1, why we additionally impose that negative values are equal zero and we set values larger than 1 equal to 1. By calculating the obscured fraction of AGN in the soft X-ray band, we can model the visible fraction of AGN $f_{\text{vis}} = 1 - f_{\text{obs}}$ and thus, the visible number density of AGN in the soft X-ray range is given by:

$$\Phi_{\text{vis}}(L_{\text{SXR}}) = f_{\text{vis}} \times \Phi_{\text{total}}(L_{\text{SXR}}) \quad (7)$$

The top row in Fig. 7 shows the soft X-ray luminosity function at $z = 0.01 - 1.6$ (different panels) in simulations without (red lines) and with dust obscuration (blue lines) and in observations from Hasinger et al. (2005) and Ebrero et al. (2009) (black stars and circles, respectively). At the high-luminosity end ($L_{\text{SXR}} > 10^{44}$ erg s $^{-1}$), obscuration does not influence our results and thus, one can see the same trends as already discussed in Fig. 6. However, turning

to the low-luminosity end, simulation results without a dust correction factor over-estimate the amount of moderately luminous AGN by up to one order of magnitude. Instead, the simulation predictions including dust obscuration can achieve a fairly good agreement with the observations. This means that our results are consistent with the observational conclusions of Hasinger (2008) supporting the adoption of a redshift-dependent dust obscuration.

Note that the adopted dust obscuration model is the same as the one in a recent study of Hirschmann et al. (2012) and similar to the one adopted in Fanidakis et al. (2012) (for the soft X-ray band), where they use the semi-analytic model of Somerville et al. (2008) and Bower et al. (2006), respectively, to study the evolution of the AGN luminosity function. In these works, they also find a good agreement between models and observations when adopting a redshift *and* luminosity dependent dust obscuration and comparing their model predictions to observed soft X-ray luminosities.

The middle and bottom rows of Fig. 7 illustrate the *hard* X-ray luminosity functions predicted by our simulations for

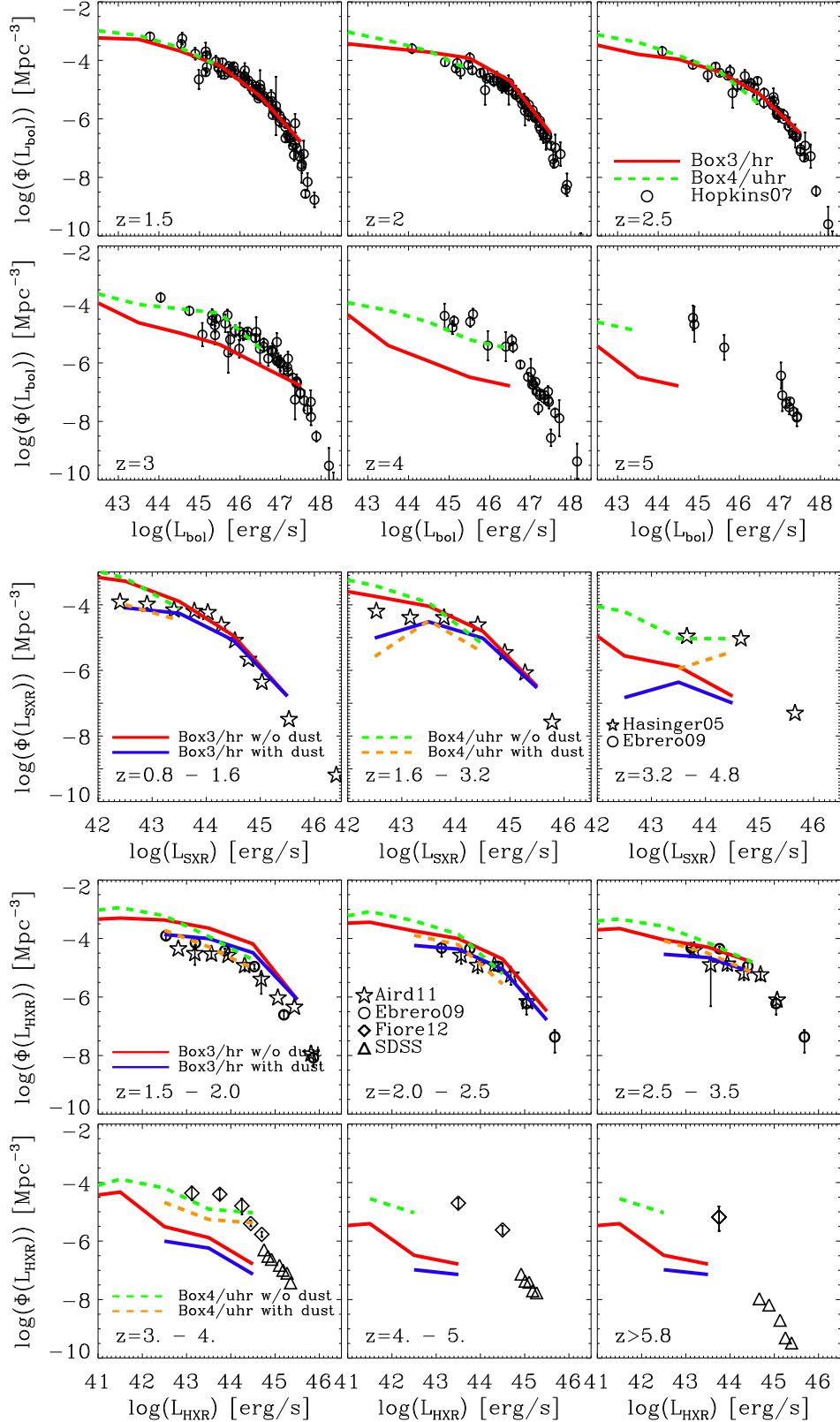


Figure 9. Evolution of the bolometric (first two rows), soft X-ray (0.5 – 2 keV, middle row) and hard X-ray (2 – 10 keV, last two rows) AGN luminosity function at $z \sim 1 - 5$. The Box3-hr (red solid line) and the Box4-uhr run (green dashed line) are compared to the observational compilation of Hopkins et al. (2007) for the bolometric luminosity and to different observational data sets for the soft and hard X-ray band (black symbols, Hasinger et al. 2005; Ebrero et al. 2009; Aird et al. 2010; Fiore et al. 2012). In addition, simulation predictions for soft and hard X-ray luminosities including dust obscuration are illustrated by blue solid and orange dashed lines for the Box3-hr and Box4-uhr run, respectively. Irrespectively of the waveband, at high redshifts $z = 3 - 4$ the amount of moderately luminous AGN in the Box4-uhr run is significantly increased resulting in an overall better match to observational data than the Box3-hr simulation.

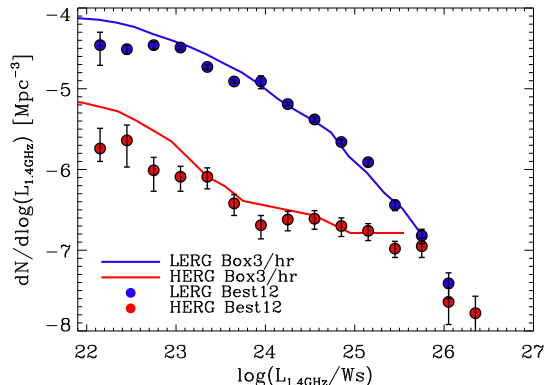


Figure 8. Radio luminosity function at $z = 0$ distinguishing between high excitation radio galaxies (red line) and low excitation radio galaxies (blue line) in the box3-hr simulation. Compared with observational data of Best & Heckman (2012) (coloured symbols), we find for both high and low excitation radio galaxies a good match of their radio luminosities.

different redshift ranges $z = 0.01 - 2.5$, compared with observational data (Ebrero et al. 2009, Aird et al. 2010, Fiore et al. 2012). The simulations (red line) are able to reproduce the high-luminosity end pretty well, and for $z < 1.2$ also the low luminosity end. However, at $z > 1.2$ the simulations over-predict the number of AGN at the low-luminosity end. One possible explanation might be again due to obscuration as even 2 – 10 keV X-ray surveys might miss a significant fraction of moderately obscured AGN (25% at $N_H = 10^{23} \text{ cm}^{-2}$) and nearly all Compton-thick AGN ($N_H > 10^{24} \text{ cm}^{-2}$, Treister et al. 2004; Ballantyne et al. 2006). From fits to the cosmic X-ray background, Gilli et al. (2007) predict that both moderately obscured and Compton-thick AGN are as numerous as unobscured AGN at luminosities higher than $\log(L_{0.5-2\text{keV}}) > 43.5$ [ergs/s], and four times as numerous as unobscured AGN at lower luminosities ($\log(L_{0.5-2\text{keV}}) < 43.5$ [ergs/s]). Also, in a study of Merloni et al. (2013, MNRAS, submitted), they investigate a complete sample of 1310 AGN from the XMM-COSMOS survey between $z = 0.3 - 3.5$ and classify them to be obscured in the hard X-ray band due to the shape of the X-ray spectrum³. Their results confirm earlier results that at each redshift there is a clear decrease of the fraction of obscured AGN with increasing luminosity. In addition (and in contrast to an optical classification), nuclear obscuration in the hard X-ray band also reveals a dependence on redshift, where the fraction of obscured AGN increases with increasing redshift. For this reason, we considered the corresponding observed, (hard X-ray) obscured fractions of AGN at a given redshift and luminosity (table 1 in Merloni et al., 2013, MNRAS, submitted). Due to the limited redshift range, we have assumed that obscured fractions at $z < 0.3$ are the same as at $z = 0.3$ and that the obscured fractions at $z > 3.5$ stay also constant. This results in a fairly good match to the observed low-luminosity

³ objects are selected to be obscured with a column density larger than $N_H > 10^{21.5} \text{ cm}^{-2}$

end for the whole redshift range (blue solid lines in Fig. 7), only at redshifts between $z = 0.5 - 1$, an additional dust obscuration tends to slightly under-estimate of the amount of moderately luminous AGN. But overall, at $z \sim 0 - 2.5$, our simulation results are roughly consistent with the existence of an obscured fraction of AGN in the hard X-ray band as suggested by observational data of Merloni et al. (2013, MNRAS, submitted), where hard X-ray dust obscuration is dependent on both redshift and luminosity.

4.3 The radio luminosity function at $z = 0$

In the last subsections, we were focusing on radiatively more efficient AGN with luminosities above 10^{43} erg/s . Radiatively less efficient AGN, however, are often observed to produce energetic, powerful radio jets and as a consequence hot X-ray cavities and thus, heat the interstellar medium. Therefore, in this section we explicitly investigate the present-day radio luminosity function by distinguishing between low excitation (“radio-mode”, LERG) and high excitation (“quasar-mode”, HERG) radio galaxies with Eddington-ratios $f_{\text{edd}} < 0.01$ and $f_{\text{edd}} > 0.01$, respectively. This allows us to study particularly all the AGN accreting at very low Eddington-ratios and to quantify their number density. To derive a radio luminosity, we follow a recent observational study of Best & Heckman (2012) who investigate a sample of 18,286 radio-loud AGN by combining data from different surveys and derive the radio luminosity functions for the first time separately for the LERGs and HERGs. In their Fig. 6, they show histograms for the ratios $(L_{\text{rad}} + L_{\text{mech}})/L_{\text{edd}}$ of the HERGs and the LERGs, which are peaking at ratios of ~ -1.6 and ~ -3 , respectively. This way, one can derive the mechanical jet luminosity L_{mech} for the HERGs and the LERGs:

$$L_{\text{mech,HERGs}} = -1.6 \times L_{\text{edd}} - L_{\text{rad}} \quad (8)$$

$$L_{\text{mech,LERGs}} = -3 \times L_{\text{edd}} - L_{\text{rad}} \quad (9)$$

L_{edd} is the maximum Eddington luminosity and L_{rad} the radiative (bolometric) luminosity of an AGN. Using the relation of Cavagnolo et al. (2010) between the 1.4 GHz radio luminosity $L_{1.4\text{GHz}}$ and the mechanical AGN jet luminosity, which is given by

$$L_{\text{mech,HERGs/LERGs}} = 10^{36} \times (L_{1.4\text{GHz}}/10^{24} \text{ WHz}^{-1})^{0.7} \text{ W}, \quad (10)$$

we can solve for the observed 1.4 GHz radio luminosity for both the HERGs and the LERGs. Fig. 8 shows the present-day radio luminosity function of the Box3-hr simulation (solid lines) and of observational data of Best & Heckman (2012) (coloured circles) distinguishing between LERGs (blue) and HERGs (red). In both observations and simulations, the LERGs provide the dominating contribution to the overall radio luminosity. We find a nearly perfect agreement between simulations and observations for both samples of radio galaxies. This implies that simulations are also able to predict reasonable radio luminosities and moreover, to reproduce the correct amount of radiatively efficient and inefficient radio AGN. This agreement also indirectly suggests that the threshold value for the accretion rate separating quasars and radio mode is a sensible one.

5 THE AGN LUMINOSITY FUNCTION AT HIGH REDSHIFTS

In this section, we focus on the AGN luminosity functions at *high* redshift (up to $z = 5$). The first two rows of Fig. 9 show the bolometric quasar luminosity function between $z = 1.5 - 5$. At $z \leq 2.5$, we find - as already discussed - a perfect agreement between the Box3-hr run (red solid line) and the observational compilation (black symbols). Above $z = 3$, however, the Box3-hr simulation significantly underestimates the amount of AGN for the whole luminosity range by up to two orders of magnitude. This can be largely seen as a consequence of a combination of both insufficient resolution for accretion in mainly low-mass black holes and too massive seed black holes (only a minor issue). Instead, for the simulation Box4-uhr (higher resolution and reduced box size, see green dashed lines in the first two rows of Fig. 9), the amount of moderately luminous AGN is significantly increased compared to the Box3-hr run resulting in a reasonably good agreement with observations at $z = 3 - 4$. Additionally, the Box4-uhr simulation correctly predicts the observed amount of moderately luminous AGN at $z \leq 2.5$, and thus, is also in agreement with the lower resolution Box3-hr run at these low redshifts. This suggests that with increasing resolution the simulation predictions seem to converge against the observational data. At $z = 5$, in order to provide a fair comparison between observations and simulations, we would need a larger volume combined with an increased resolution than what we currently have in the Box4-uhr or in the Box3-hr simulation. For the present, this, however, represents a great challenge for the currently available computational power. In a recent study of DeGraf et al. (2012), they have performed cosmological simulation (using Gadget2 with a similar model for black hole growth) with a large box-size of 533 Mpc/h, but only run down to $z = 5$. When considering the AGN luminosity function at $z = 5$ and $z = 6$ they obtain a fairly good agreement to observational data at these high redshift.

In Fig. 9 we additionally show the evolution of the soft (third row) and hard (fourth and fifth rows) X-ray luminosity function at high redshifts, between $z = 0.8 - 4.8$ and $z = 1.5 - 5.8$, respectively. Up to a redshift of $z = 3.2$ and $z = 3.5$, respectively, the Box3-hr simulation accounting for dust obscuration (blue solid line) provides a reasonably good match to the observational data and is also in agreement with the corresponding Box4-uhr run (orange dashed line). At higher redshifts, in both the soft X-ray band and in the hard X-ray band, the AGN number densities are again under-estimated for the entire luminosity range by up to two orders of magnitude in the Box3-hr run (with and without accounting for dust obscuration, blue and red solid lines). In contrast, in the Box4-uhr simulation (green and orange dashed lines), the amount of moderately luminous is again significantly increased. Therefore, this simulation (when neglecting dust obscuration) results in a better agreement with observational data up to $z \sim 4$. Going to redshifts above $z = 4$ in the hard X-ray band, the Box4-uhr simulation again provides a too small volume to produce enough AGN with X-ray luminosities above $10^{43.5}$ erg/s and to achieve a fair comparison with observational data.

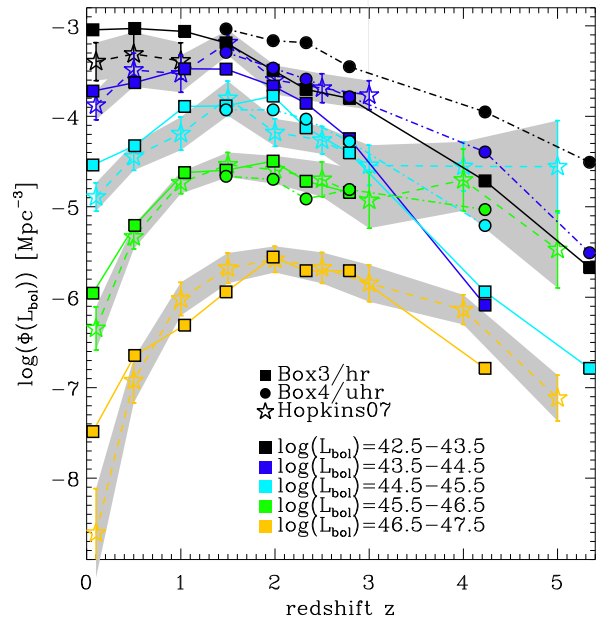


Figure 10. Co-moving number density evolution of AGN binned in different bolometric luminosity bins (indicated by different colours) in simulations (filled squares and solid lines: box3/hr; filled circles and dashed-dotted lines: box4/uhr) and in the observational compilation of Hopkins et al. (2007) (open stars with dashed lines and the grey shaded areas). Our Simulations are able to naturally predict the observed anti-hierarchical trend.

6 ANTI-HIERARCHICAL GROWTH OF BLACK HOLES

6.1 Co-moving number density evolution of AGN

In the sections 4 and 5 we have shown that a combination of the Box3-hr and the Box4-uhr simulation runs can reproduce the evolution of the AGN luminosity from $z = 4$ to $z = 0$ reasonably well. This implies that our simulations should also be able to naturally reproduce the observed “anti-hierarchical” or “downsizing” trend in black hole growth within the framework of a hierarchical structure formation scenario. As described in the introduction, the term “downsizing” refers to the observational result that the number density of luminous AGN peaks before successively less luminous AGN. This is visualised in Fig. 10 showing the redshift evolution of the AGN number densities binned in different bolometric luminosity bins (different coloured lines as indicated in the legend). The observational data of Hopkins et al. (2007) (open stars with the dashed lines and the grey shaded area) reveal a time evolution of the peaks of the luminosity curves being characteristic for the downsizing trend. At $z < 3$, the Box3-hr run (filled squares with solid lines) matches the observations very well, while at higher redshifts and for moderately luminous AGN the Box4-uhr run (filled circles with dotted-dashed lines) agrees better with the observations, but only for moderately luminous AGN (due to resolution). This clearly shows that the simulations can correctly capture the observed time evolution of the peaks of the different luminosity curves, and thus,

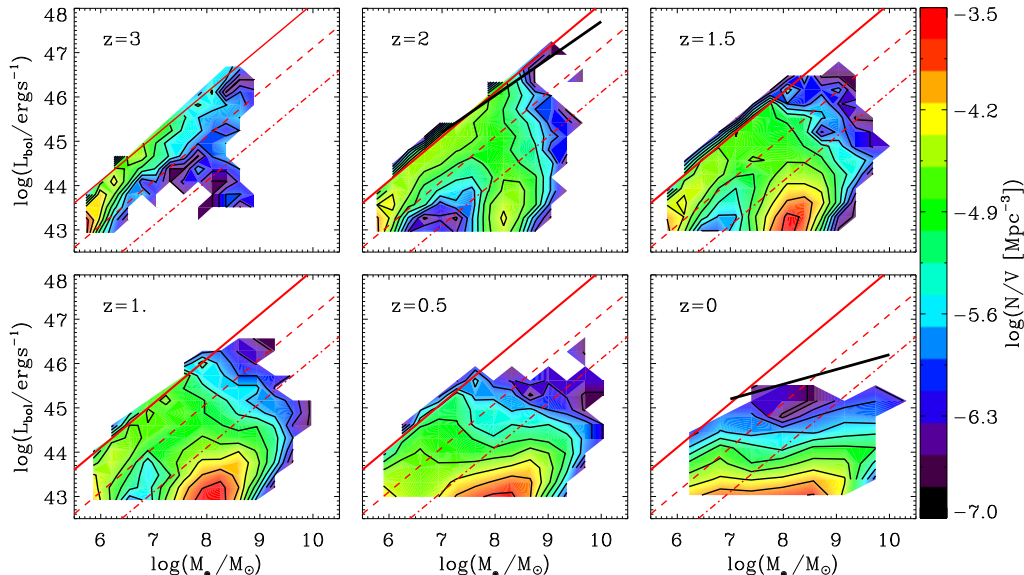


Figure 11. 2-dimensional histograms (number density is colour-coded) of the bolometric luminosity-black hole mass-plane at different redshifts $z = 3 - 0$. The red lines indicate an accretion at the Eddington rate (solid line), at 1/10 (dashed line) and at 1/100 (dotted-dashed line) of the Eddington rate. Black lines correspond to Eddington limits found by observations (Steinhardt & Elvis 2010). High redshifts are dominated by black holes accreting at or close to the Eddington rate, while going to lower redshifts there is an increasing contribution of massive black holes accreting at very low Eddington-ratios.

the corresponding downsizing trend. The strong decrease of luminous AGN (see green and yellow curves) at low redshift $z < 2$ is mainly due to the decreasing cold gas content in the vicinity of the massive black holes (e.g. due to AGN feedback), i.e. if a merger is going to happen it is preferentially a ‘dry’ merger not triggering any significant AGN activity. Instead, moderately luminous AGN probably are either low-mass black holes with high accretion rates or massive black holes, which are - due to the small amount of cold gas which is left - accreting at low rates and which have most likely been very luminous in the past. This will be discussed and analysed in more detail in the next sections.

6.2 Implications on the connection between black hole mass and AGN luminosity

We now examine consequences and implications of a downsizing trend on the connection between black hole mass, the Eddington ratio and the bolometric luminosity of AGN. Fig. 11 shows a 2-dimensional histogram (AGN number density is colour-coded) of the bolometric AGN luminosity-black hole mass plane at different redshift steps $z = 3 - 0$ for the Box3-hr simulation. The red lines help to visualise an accretion at the (maximum) Eddington rate (solid line), at 1/10 (dashed line) and at 1/100 (dotted-dashed line) of the Eddington rate. At $z = 3$, the majority of the black holes with masses up to $M_{\bullet} \leq 10^9 M_{\odot}$ is accreting at or at least very close to the Eddington rate ($0.1 < f_{\text{edd}} < 1$), i.e. for these high redshifts, the AGN luminosity is approximately linearly related with black hole mass. Turning to lower redshifts ($z \leq 2$), the number density of AGN with massive black holes ($M_{\bullet} > 10^9 M_{\odot}$) has increased relative to $z = 3$. The relation between black hole mass and bolometric luminosity becomes much broader, the linear relation found

at higher redshifts is broken, and black holes with masses $M_{\bullet} \sim 10^8 M_{\odot}$ can now also power moderately luminous AGN with $L_{\text{bol}} \sim 10^{43}$ erg/s as they are accreting with Eddington ratios below $f_{\text{edd}} < 0.01$. The probability for black holes with $M_{\bullet} > 10^7 M_{\odot}$ to accrete at Eddington ratios below $f_{\text{edd}} = 0.01$ is even higher than to accrete at larger Eddington ratios. These black holes most likely are relics from an earlier, more active phase with higher accretion rates, which undergo at later times a ‘blow-out’ or ‘fading’ phase, where the gas gets ejected out of the central regions around the black hole due to AGN/radio mode feedback (and so the gas density in the vicinity of the black hole is reduced, see the discussion in section 6.3). This process is shown in different studies of e.g. Hopkins et al. (2008) who perform a detailed analysis of a large set of isolated merger simulations. They present typical light curves of AGN triggered by mergers, with a first phase of high accretion close to the Eddington rate, followed by a power-law decline in the accretion rate. We expect that this is broadly traced within our cosmological simulation and plan to study the detailed light curves in a higher resolution simulation in a follow-up study. Finally, Fig. 11 shows that the number density of luminous AGN ($L_{\text{bol}} > 10^{45}$ erg/s) is significantly smaller (almost completely suppressed) at $z = 0$ than at $z = 2$. This is mainly due to the available gas content, which gets reduced particularly in massive galaxies and their relatively high star formation, over cosmic time (due to feedback from the AGN itself). This is also consistent with observational results of e.g. Steinhardt & Elvis (2010) (see black solid lines) and Kelly & Shen (2013), who find that the probability of massive black holes accreting close to the Eddington-rate is significantly reduced at low redshift.

Fig. 12 shows the redshift evolution of the Eddington ratio distributions for the Box3-hr simulation (different

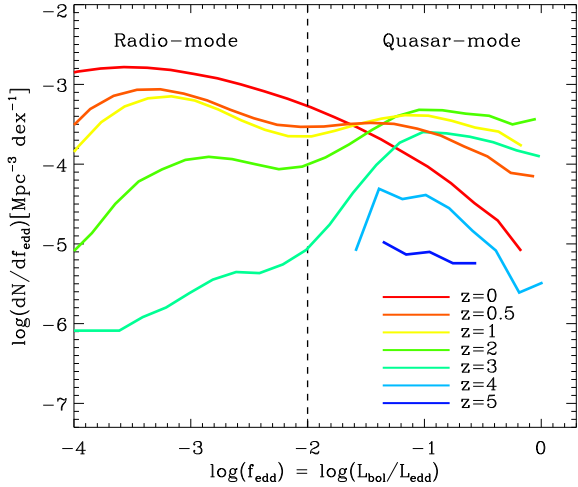


Figure 12. Eddington ratio distributions at different redshift steps $z = 0 - 5$ (indicated by coloured lines) for the Box3-hr simulation. The vertical dashed line visualises the distinction between radio- and quasar-mode adopted in the model. The peaks of the distributions are shifted towards lower Eddington-ratios with decreasing redshift, what is in qualitative agreement with observational studies (Vestergaard 2003; Kollmeier et al. 2006; Kelly et al. 2010; Schulze & Wisotzki 2010).

coloured lines illustrate different redshift steps). The vertical dashed line visualises the (assumed) division between the radio- and quasar- mode in the simulation code. Consistent with our previous analysis, and typical limits of observational samples, we consider only AGN with bolometric luminosities larger than 10^{43} erg/s. The simulated fraction of AGN which are accreting at small Eddington ratios ($f_{\text{edd}} < 0.01$) increases strongly with decreasing redshift and thus, the peaks of the distribution curves are clearly shifted towards smaller Eddington ratios with decreasing redshift – a typical implication of the downsizing trend: at $z = 4$, the distribution peaks at $f_{\text{edd}} \sim 0.1$, while at $z = 0$ the peak is located around $f_{\text{edd}} \sim 0.001$. This illustrates the same trend we discussed for Fig. 11: at later times black holes spend less time accreting at the Eddington rate, but mainly reside in a decline dominated “blowout” accretion phase. As a further consequence, the number of black holes accreting close to the Eddington-rate is low at $z = 0$ ($\log(dN/df_{\text{edd}}) \sim -5 \text{ Mpc}^{-3} \text{ dex}^{-1}$), while at high redshifts ($z = 1 - 3$) a large number of black holes ($\log(dN/df_{\text{edd}}) \sim -3.5 \text{ Mpc}^{-3} \text{ dex}^{-1}$) are preferentially accreting within a broad range of Eddington ratios $0.01 < f_{\text{edd}} < 1$. Overall, the majority of AGN at $z = 0$ are hardly radiating at or near the Eddington limit, which is in qualitative agreement with several observational studies (Vestergaard 2003; Kollmeier et al. 2006; Kelly et al. 2010; Schulze & Wisotzki 2010; Steinhardt & Elvis 2010; Kelly & Shen 2013). For example, Kelly et al. (2010) find that the Eddington ratio distribution (using broad-line quasars between $z = 1 - 4$) peaks at an Eddington ratio of $f_{\text{edd}} = 0.05$.

Furthermore, in Fig. 13 we present a quantitative comparison of simulated Eddington-ratios with observational data: the simulated mean Eddington-ratios of AGN with luminosities above 10^{43} erg/s are plotted versus redshift (see

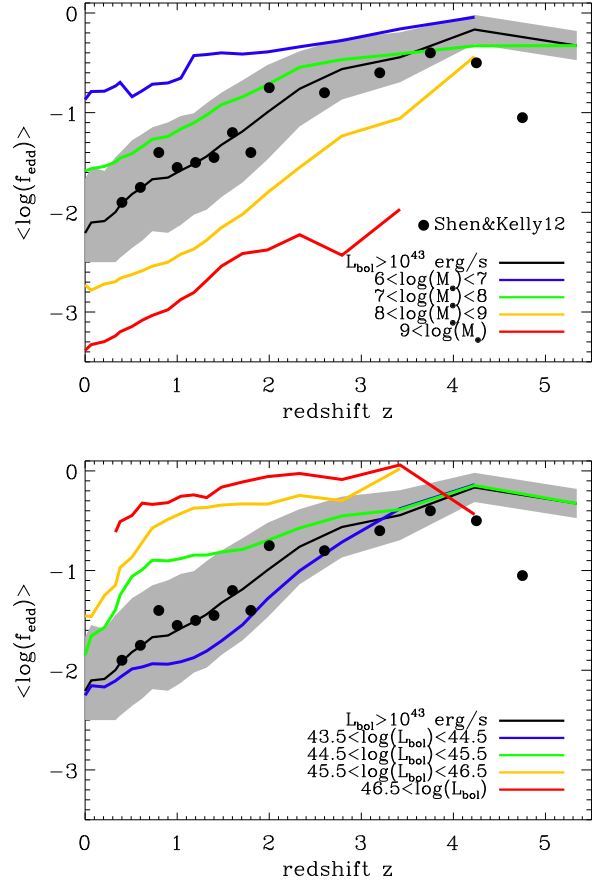


Figure 13. Redshift evolution of the mean Eddington-ratios for the Box3-hr run (black solid lines; grey shaded areas indicate the $1-\sigma$ scatter) divided into different black hole mass bins (coloured lines in the top panel) and into different bolometric luminosity bins (coloured lines in the bottom panel). The simulated predictions match the observational mean Eddington-ratios reasonably well at $z \leq 4$.

black line with grey shaded areas in both panels) and compared to observational data of Shen & Kelly (2012) (black, filled circles). In both simulations and observations, the mean Eddington-ratios are decreasing with decreasing redshift and we find a nearly perfect agreement between them at $z \leq 4$. Additionally, in the simulations, we have divided the AGN sample into different black hole mass bins (coloured lines in the top panel of Fig. 13) and different AGN luminosity bins (coloured lines in the bottom panel of Fig. 13). This illustrates that on average, for the entire redshift range since $z \sim 4$, lowest mass black holes (blue line in the top panel) and most luminous AGN (red line in the bottom panel) accrete at the highest Eddington-ratios ($0.1 < f_{\text{edd}} < 1$). In contrast, the most massive black holes (red line in the top panel) and the lowest luminous AGN (blue line in the bottom panel) have the lowest mean Eddington-ratios. This behaviour is consistent with Fig. 11.

Overall, we want to point out that the interplay between black hole mass, AGN luminosity and Eddington-ratio, we have discussed in this section, is in good qualitative agreement with previous studies of Fanidakis et al. (2012) and

Hirschmann et al. (2012) who also reproduced the downsizing trend in black hole growth, but by using semi-analytic models. This may again confirm that such a connection between black hole masses and AGN luminosities seems to be a necessary condition for reproducing a downsizing trend in black hole growth.

6.3 Physical origin of the downsizing trend in our simulations

A common problem of all currently existing, large cosmological simulations is that they are not able to capture the detailed physical processes of gas accretion in the close vicinity of the black hole due to too low resolution as a result of the (up to now) limited computational power. Besides, the physical description of black hole accretion is also more complicated than typically assumed in large-scale simulations (e.g. there is no spherical symmetry in reality, see King & Nixon 2013). Thus, a very rough approximation for the accretion process is generally adopted when performing large-scale simulations as we have described earlier in section 2.2. Still, as we have seen in the course of this study, simulations seem at least to be able to reproduce the right trends of how black holes assemble their mass and appear as an AGN despite their relatively low spatial and mass resolution (compared to the physical scales at which the gas accretion is actually happening). In other words, the general scheme in our simulations is able to capture the essence of black hole growth “in reality”. Therefore, to better understand the *physical reason* for automatically reproducing the downsizing trend in our simulations, we directly investigate the different gaseous quantities, as the density, the sound speed, which is proportional to the gas temperature and the relative velocity (between the gas particles and the black hole), which are contributing to the estimation of the Bondi-accretion rate in the code given by Eq. 1 (by averaging over all the gas particles within the numerically resolved accretion region of the black hole).

Fig. 14 shows the mean (solid lines) and the corresponding $1\text{-}\sigma$ scatter (dashed lines) of the gas density (top row), of the gas temperature (middle row) and of the relative gas velocity (bottom row) within the numerically resolved accretion region versus black hole mass at $z = 2.8$ (green), $z = 1$ (orange) and $z = 0$ (red). All quantities are in physical units. The mean relative gas velocity was calculated by averaging over the relative velocities between the black hole and all the gas particles of x , y and z -components and then by computing the norm of the mean x , y and z -velocity. To be consistent with our earlier results for the bolometric AGN luminosities, we have only considered AGN with $\log(L_{\text{bol}}) > 43$ [erg/s] (left column) and additionally distinguished between an accretion in the quasar (middle column) and the radio mode (right column), depending on the Eddington-ratio. Irrespectively of the redshift, both the mean gas temperature T and the mean relative velocity V_{rel} are increasing, while the gas density ρ is decreasing with increasing black hole mass when considering *all* AGN (left column). This means – when taking into account equation 1 – that at any redshift the “relative” accretion rates (e.g. accretion rate / M_{\bullet}^2) tend to decrease with increasing black hole mass. This can explain the black hole mass dependence of the AGN number density at a given redshift as seen in the

AGN luminosity-black hole mass plane: AGN number densities of massive black holes peak at low Eddington-ratios and vice versa (see Fig. 11).

Turning now to the redshift dependence of the average gas quantities (different coloured lines in the left column of Fig. 14), we find for massive black holes ($M_{\bullet} > 5 \times 10^6 M_{\odot}$) a significant decrease of the mean gas density by almost two orders of magnitude from $z = 2.8$ to $z = 0$, what most likely causes a decrease of the relative accretion rates at a given black hole mass towards lower redshifts (even if the gas temperature, and thus the sound speed, is slightly decreasing towards lower redshifts). This can, therefore, explain the decrease in the number density of very luminous AGN with $\log(L_{\text{bol}}) \geq 46$ [erg/s] (i.e. very massive black holes $M_{\bullet} \geq 10^8 M_{\odot}$ accreting at high Eddington-ratios) over cosmic time (since $z \sim 2$, see yellow and green curves in Fig. 10). A further consequence of the decreasing accretion rates of massive black holes with decreasing redshift is that these objects have now preferentially moderate luminosities and thus, can contribute to the weakly increasing number density of *moderately luminous* AGN with evolving time (see black and dark/light blue lines in Fig. 10).

Instead, for low mass black holes ($M_{\bullet} < 5 \times 10^6 M_{\odot}$), the gas temperature and density do not change significantly with redshift, whereas the relative velocity (between the gas and the black hole) increases at progressively higher redshifts. The latter point is due to the fact that at high redshift small galaxies are not relaxed yet, and so the relative accretion rates get strongly suppressed in reflection of the increased relative velocity between the black hole in the centre of the halo and the surrounding gas. In other words, the relative gas accretion rates of low mass black holes are on average lower at higher redshifts, i.e. low mass black holes accrete relatively more at present. Note that this is not caused by a too low resolution, as when considering our higher-resolved simulation (Box4-ubr), this effect remains. The increasing accretion in low-mass black holes with decreasing redshift can also contribute to the weak, but continuous increase of the number densities of moderately luminous AGN (see black and dark blue lines in Fig. 10) – in addition to the massive black holes accreting at low Eddington-ratios.

Overall, this behaviour is a result of the interplay of radio- and quasar-mode accretion as adopted in our model: At high redshifts $z > 2$ for the whole mass range and at lower redshifts for low mass black holes ($M_{\bullet} \leq 5 \times 10^6 M_{\odot}$), the gaseous quantities reveal the same behaviour as in the quasar mode (see middle column of Fig. 14). This is the dominating accretion mechanism for these regimes and thus, is responsible for the overall decrease of the mean relative velocities of low mass black holes towards low redshifts (and thus, increasing the amount of moderately luminous AGN). Instead, for low redshifts $z \leq 1$ and more massive black holes ($M_{\bullet} \geq 5 \times 10^6 M_{\odot}$), the accretion at the radio-mode is dominating the gaseous quantities (right column of Fig. 14). In particular, the stronger feedback in the radio-mode leads to a strong decreasing gas density with increasing black hole mass and decreasing redshift. This is not the case for an accretion at the quasar-mode, where at $z = 0$ the gas density is increasing with increasing black hole mass and for the most massive black holes, the gas density tends to be even slightly larger than at higher redshifts. This clearly shows that the radio-mode feedback is essential for regulating black hole

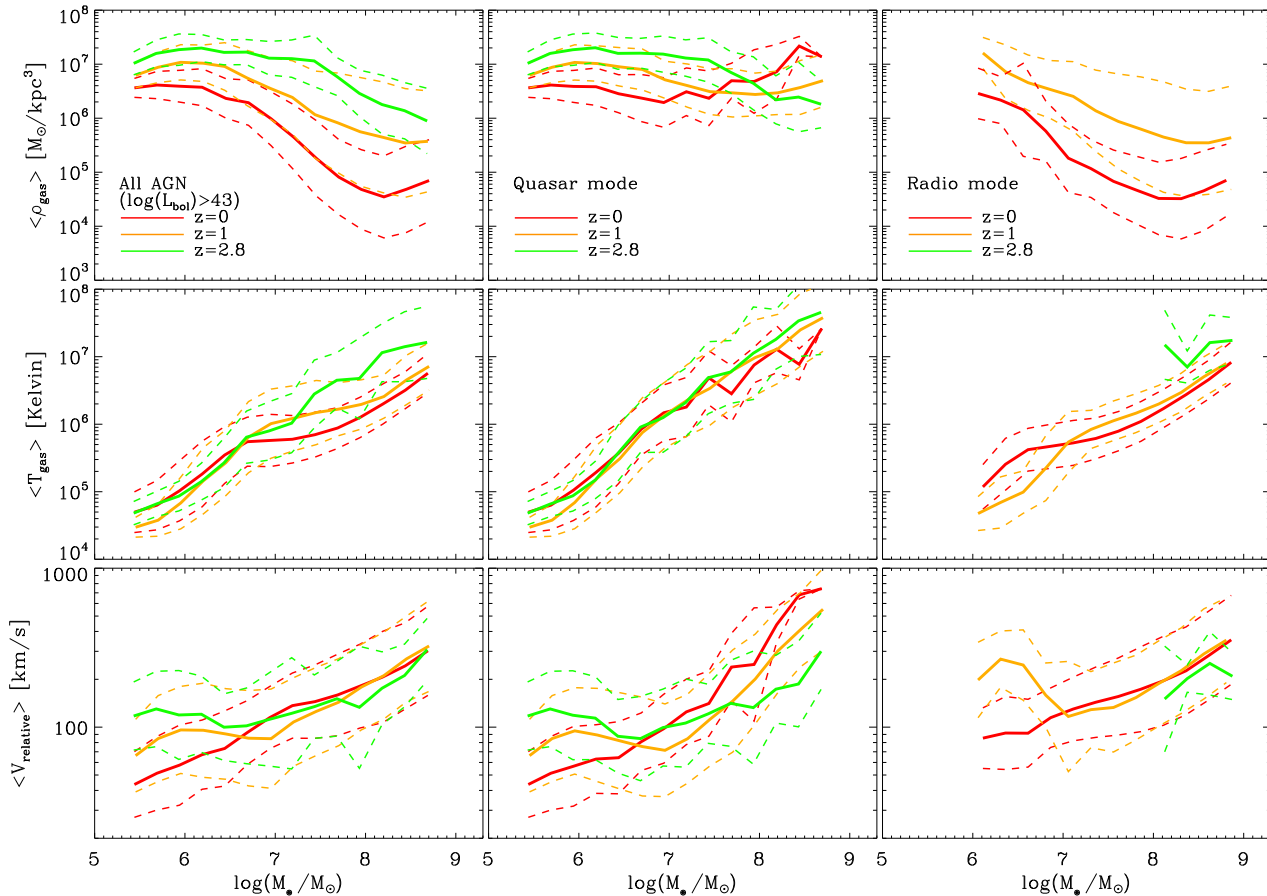


Figure 14. Mean gas density (top row), mean gas temperature (middle row) and mean relative gas velocity between the black hole and the gas particles (bottom row) within the numerically resolved accretion region versus black hole mass at $z = 2.8$ (green lines), $z = 1$ (orange lines) and $z = 0$ (red lines). We have considered only AGN with $\log(L_{\text{bol}}) > 43$ [erg/s] (left column) and additionally distinguished between the quasar (middle column) and the radio mode (right column), depending on the Eddington ratio. Irrespectively of the redshift, the gas temperature and relative velocity is increasing, while the gas density is slightly decreasing with increasing black hole mass.

growth rates at late times (by strongly depleting the gas in the vicinity of a black hole and thus, inhibiting further gas inflows) and therefore, for suppressing the amount of luminous AGN at low redshift. However, we have seen before that the present-day number densities of luminous AGN tend to be slightly over-estimated in our simulations (see Figs. 10, 6, 7). This signals a too weak efficiency of our radio-mode feedback as already discussed for the present-day black hole mass and stellar mass function (see Figs. 2, 3).

To summarise, we find that the downsizing trend in the AGN number density evolution and thus, the black hole accretion, in our simulations is mainly caused by “global” gas-physical properties in the vicinity of the resolved accretion region and not necessarily by the “local” gas properties within the Bondi accretion radius. Interestingly, this is in agreement with detailed, high-resolved (spatial resolution of 200 pc) 3D simulations of black hole accretion, which indicate that the black hole accretion is mainly driven by large-scale gas properties beyond 1 kpc (G. Novak, personal communication; Novak, Durier & Babul, in prep.) and not by the local gas properties. Essentially, we have demonstrated that a combination of both a decreasing mean gas density of

black holes with increasing black hole mass and decreasing redshift and a lower mean relative velocity of low mass black holes at lower redshifts is causing the downsizing trend in the AGN number density evolution.

7 SUMMARY AND DISCUSSION

In this study, we have analysed a subset of hydrodynamic, fully cosmological simulations from the Magneticum Pathfinder simulation set (Dolag et al., in prep.) focusing on statistical properties of black holes and AGN from $z = 5$ down to $z = 0$, in particular on the evolution of the AGN luminosity function and its corresponding downsizing trend in black hole growth. The simulations are based on the SPH code Gadget3 (Springel 2005) and contain radiative gas cooling, a spatially uniform UV background and a multi-phase model for star formation with the associated feedback processes (Springel & Hernquist 2003). The simulations also include a detailed model of chemical evolution according to Tornatore et al. (2007), where metals are released by SNII, SNIa explosions and AGB stars. In addition, the prescriptions for black hole growth and feedback from AGN are

based on the models presented in Springel et al. (2005a) and Di Matteo et al. (2005), but contain the same modifications as in the study of Fabjan et al. (2010) and some new changes (as discussed in section 2.2). We have considered two simulation runs, one with a large co-moving volume of $(128 \text{ Mpc/h})^3$ and one with a smaller volume of $(48 \text{ Mpc/h})^3$ but a higher resolution. We now summarise our main results:

1. Consistent with previous studies (e.g. Di Matteo et al. 2008), our simulations are in reasonably good agreement with the observed present-day black hole-stellar mass relation and the black hole mass function, although the high-mass end is slightly over-estimated due to too inefficient radio mode feedback. The latter point is also true for the stellar mass function, i.e. the simulations tend to produce too many too massive galaxies (with too massive black holes) at low redshifts. The main growth of black holes is found to occur before $z \sim 1$ when considering the evolution of the black hole mass function, which is already in place at $z \sim 1$. This is also consistent with the cosmic evolution of black hole accretion rates, which peak around $z \sim 1.5$ and start to strongly decline towards lower redshifts.

2. Our simulations can successfully reproduce the observed bolometric AGN luminosity function up to $z \sim 2.5$ (Hopkins et al. 2007). For moderately luminous AGN this is consistent with a previous study of Degraf et al. (2010), *but the high luminosity end ($L_{\text{bol}} \geq 10^{45} \text{ erg/s}$) can be probed – for the first time – in our large-volume simulation.* At higher redshifts (up to $z \sim 5$), however, the large-volume simulation predicts a too small amount of AGN due to resolution effects. But turning to a smaller volume with higher resolution helps to increase the amount of moderately luminous AGN in reasonably good agreement with observations. We want to point out that the small-volume simulation can also match the low-luminosity end of the AGN luminosity function at low redshifts, i.e. higher resolution simulations seem to converge against the observational data.

3. Besides the bolometric luminosities, we have additionally extended our model predictions for obscuration to compare them directly with recent soft and hard X-ray measurements of the AGN luminosity function. When adopting an empirically motivated dust obscuration model, where obscuration of AGN is dependent on both, redshift and luminosity, we find a reasonably good agreement between the large-volume simulation and observations up to $z \sim 2.5 - 3$ and up to a redshift $z = 4 - 5$ for the small-volume simulation.

Dividing our AGN in low and high excitation state, we are also able to reproduce observed number densities of present day LERGs/HERGs radio galaxies, implying that the simulations can successfully capture the correct amount of radiatively efficient and inefficient AGNs.

4. As a consequence of points 2. and 3., a combination of both simulation runs (small- and large-volume) can successfully reproduce the co-moving number density evolution of AGN up to $z = 4 - 5$, and therefore, naturally predict the characteristic, observed downsizing trend within a hierarchical structure formation scenario. The strong decline of luminous AGN with decreasing redshift (since $z = 2$) can be attributed to the gas density in the vicinity of a (massive) black hole, which gets successively depleted with evolving time, particularly as a consequence of the radio-mode feed-

back. Therefore, the gas inflow towards a massive black hole is inhibited and its luminosity starts to fade (and can then contribute to the amount of moderately luminous AGN). This also explains why massive black holes preferentially accrete at low Eddington-ratios at $z < 3$.

The continuous increase of moderately luminous AGN over time can, instead, be seen a result of both massive black holes in their “fading” phase and low mass black holes as they tend to have higher accretion rates towards lower redshifts due to decreasing mean relative velocities between the black hole and the surrounding gas with decreasing redshift.

5. Finally, we find that the downsizing behaviour implies that the peaks of the Eddington ratio distributions are shifted towards successively smaller Eddington ratios with decreasing redshift – a trend which has also been shown in observational studies. The number of black holes accreting close to the Eddington-rate is more than one order of magnitude smaller at $z = 0$ than at high redshifts ($z = 1 - 3$), where the black holes are preferentially accreting within a broad range of Eddington ratios $0.01 < f_{\text{edd}} < 1$. Besides, our simulations can successfully predict the observed evolution of the mean Eddington-ratio for AGN more luminous than $L_{\text{bol}} > 10^{43} \text{ [erg/s]}$. These implications of the downsizing behaviour are in qualitative agreement with predictions from semi-analytic models (see e.g. Fanidakis et al. 2012; Hirschmann et al. 2012).

Despite the overall success of the simulations being in reasonably good agreement with observational data we should keep in mind that this is attained despite of the rather crude, approximate and numerically limited description of black hole accretion, energy extraction and thermalisation (even if high-resolution simulations of black hole accretion indicate an independence of the black hole accretion on local gas properties up to 1 kpc around the black hole; Novak, Durier and Babul, in prep.). But nevertheless, this study nicely demonstrates that the observed downsizing trend in black hole growth is not contradictory with a hierarchical structure formation model (and thus qualitatively consistent with the results of semi-analytic models as shown in Bonoli et al. 2009; Fanidakis et al. 2012; Hirschmann et al. 2012), but instead is a “natural” outcome due to specific baryon processes. Besides the “downsizing” trend, there exist many more unresolved questions about black hole growth and AGN evolution which can be easily assessed in our simulations. Therefore, in forthcoming studies, we plan to examine the connection between AGN and their host galaxy properties, AGN clustering properties and typical AGN light curves (of differently luminous AGN) what may particularly illuminate our current understanding of how strongly galaxies and black holes are co-evolving and what are the main trigger mechanisms for AGN activity (if there are any), what is – up to now – a major unresolved open issue in understanding black hole growth and AGN evolution.

ACKNOWLEDGMENTS

We thank Andrea Merloni, Francesco Shankar, James Aird, Jacobo Ebrero and Fabrizio Fiore for providing us with observational data and Andrea Merloni, Greg Novak and Rachel Somerville for fruitful discussions.

This research was supported by the DFG Cluster of

Excellence 'Origin and structure of the universe'. M.H. acknowledges financial support from the European Research Council under the European Community's Seventh Framework Programme (FP7/2007-2013)/ERC grant agreement n. 202781. S.B. acknowledges financial support from the European Commission's Framework Programme 7, through the Marie Curie Initial Training Network Cosmo-Comp (PITN-GA-2009-23856), the PRIN-MIUR-2009 grant "Tracing the growth of structures in the Universe" and the PD51-INFN grant.

REFERENCES

- Aird J., Nandra K., Laird E. S., Georgakakis A., Ashby M. L. N., Barmby P., Coil A. L., Huang J., Koekemoer A. M., Steidel C. C., Willmer C. N. A., 2010, *MNRAS*, 401, 2531
- Ballantyne D. R., Shi Y., Rieke G. H., Donley J. L., Papovich C., Rigby J. R., 2006, *ApJ*, 653, 1070
- Barai P., Viel M., Murante G., Gaspari M., Borgani S., 2013, *ArXiv e-prints*
- Barger A. J., Cowie L. L., 2005, *ApJ*, 635, 115
- Barger A. J., Cowie L. L., Capak P., Alexander D. M., Bauer F. E., Brandt W. N., Garmire G. P., Hornschemeier A. E., 2003, *ApJ*, 584, L61
- Bellovary J., Volonteri M., Governato F., Shen S., Quinn T., Wadsley J., 2011, *ApJ*, 742, 13
- Best P. N., Heckman T. M., 2012, *MNRAS*, 421, 1569
- Blumenthal G. R., Faber S. M., Primack J. R., Rees M. J., 1985, *Nature*, 313, 72
- Bondi H., 1952, *MNRAS*, 112, 195
- Bondi H., Hoyle F., 1944, *MNRAS*, 104, 273
- Bongiorno A. e. a., 2012, *MNRAS*, 427, 3103
- Bonoli S., Marulli F., Springel V., White S. D. M., Branchini E., Moscardini L., 2009, *MNRAS*, 396, 423
- Booth C. M., Schaye J., 2009, *MNRAS*, 398, 53
- Booth C. M., Schaye J., 2011, *MNRAS*, 413, 1158
- Bower R. G., Benson A. J., Malbon R., Helly J. C., Frenk C. S., Baugh C. M., Cole S., Lacey C. G., 2006, *MNRAS*, 370, 645
- Bromley J. M., Somerville R. S., Fabian A. C., 2004, *MNRAS*, 350, 456
- Bundy K., Ellis R. S., Conselice C. J., 2005, *ApJ*, 625, 621
- Burkert A., Tremaine S., 2010, *ApJ*, 720, 516
- Cavagnolo K. W., McNamara B. R., Nulsen P. E. J., Carilli C. L., Jones C., Birzan L., 2010, *ApJ*, 720, 1066
- Chabrier G., 2003, *PASP*, 115, 763
- Chandrasekhar S., 1943, *ApJ*, 97, 255
- Choi E., Ostriker J. P., Naab T., Johansson P. H., 2012, *ApJ*, 754, 125
- Cisternas M., Jahnke K., Inskip K. J., Inskip 2010, in *IAU Symposium Vol. 267 of IAU Symposium, Quasars Do Not Live in Merging Systems: No Enhanced Merger Rate at $z < 0.8$* . pp 326–326
- Cowie L. L., Barger A. J., Bautz M. W., Brandt W. N., Garmire G. P., 2003, *ApJ*, 584, L57
- Cristiani S., Alexander D. M., Bauer F., Brandt W. N., Chatzichristou E. T., Fontanot F., Grazian A., Koekemoer A., Lucas R. A., Monaco P., Nonino M., Padovani P., Stern D., Tozzi P., Treister E., Urry C. M., Vanzella E., 2004, *ApJ*, 600, L119
- Croom S. M., Smith R. J., Boyle B. J., Shanks T., Miller L., Outram P. J., Loaring N. S., 2004, *MNRAS*, 349, 1397
- Croton D. J., 2006, *MNRAS*, 369, 1808
- Debuhr J., Quataert E., Ma C.-P., 2012, *MNRAS*, 420, 2221
- DeGraf C., Di Matteo T., Khandai N., Croft R., Lopez J., Springel V., 2012, *MNRAS*, 424, 1892
- Degraf C., Di Matteo T., Springel V., 2010, *MNRAS*, 402, 1927
- Degraf C., Di Matteo T., Springel V., 2011, *MNRAS*, 413, 1383
- Di Matteo T., Colberg J., Springel V., Hernquist L., Sijacki D., 2008, *ApJ*, 676, 33
- Di Matteo T., Khandai N., DeGraf C., Feng Y., Croft R. A. C., Lopez J., Springel V., 2012, *ApJ*, 745, L29
- Di Matteo T., Springel V., Hernquist L., 2005, *Nature*, 433, 604
- Dolag K., Vazza F., Brunetti G., Tormen G., 2005, *MNRAS*, 364, 753
- Drory N., Bender R., Feulner G., Hopp U., Maraston C., Snigula J., Hill G. J., 2004, *ApJ*, 608, 742
- Ebrero J., Carrera F. J., Page M. J., Silverman J. D., Barcons X., Ceballos M. T., Corral A., Della Ceca R., Watson M. G., 2009, *A&A*, 493, 55
- Efstathiou G., Rees M. J., 1988, *MNRAS*, 230, 5P
- Ellison S. L., Patton D. R., Mendel J. T., Scudder J. M., 2011, *MNRAS*, 418, 2043
- Ellison S. L., Patton D. R., Simard L., McConnachie A. W., 2008, *AJ*, 135, 1877
- Fabjan D., Borgani S., Tornatore L., Saro A., Murante G., Dolag K., 2010, *MNRAS*, 401, 1670
- Fan X., Hennawi J. F., Richards G. T., Strauss M. A., Schneider D. P., Donley J. L., Young J. E., Annis J., Lin H., Lampeitl H., Lupton R. H., Gunn J. E., Knapp G. R., 2004, *AJ*, 128, 515
- Fanidakis N., Baugh C. M., Benson A. J., Bower R. G., Cole S., Done C., Frenk C. S., Hickox R. C., Lacey C., Del P. Lagos C., 2012, *MNRAS*, 419, 2797
- Ferland G. J., Korista K. T., Verner D. A., Ferguson J. W., Kingdon J. B., Verner E. M., 1998, *PASP*, 110, 761
- Ferrarese L., Merritt D., 2000, *ApJ*, 539, L9
- Fiore F., Brusa M., Cocchia F., Baldi A., Carangelo N., Ciliegi P., Comastri A., La Franca F., Maiolino R., Matt G., Molendi S., Mignoli M., Perola G. C., Severgnini P., Vignali C., 2003, *A&A*, 409, 79
- Fiore F., Puccetti S., Grazian A., Menci N., Shankar F., Santini P., Piconcelli E., Koekemoer A. M., Fontana A., Boutsia K., Castellano M., Lamastra A., Malacaria C., Feruglio C., Mathur S., Miller N., Pannella M., 2012, *A&A*, 537, A16
- Fontana A., Salimbeni S., Grazian A., Giallongo E., Pentericci L., Nonino M., Fontanot F., Menci N., Monaco P., Cristiani S., Vanzella E., de Santis C., Gallozzi S., 2006, *A&A*, 459, 745
- Gabor J. M., Bournaud F., 2013, *ArXiv e-prints*
- Gebhardt K., Bender R., Bower G., Dressler A., Faber S. M., Filippenko A. V., Green R., Grillmair C., Ho L. C., Kormendy J., Lauer T. R., Magorrian J., Pinkney J., Richstone D., Tremaine S., 2000, *ApJ*, 539, L13
- Genzel R., Eckart A., 1999, in H. Falcke, A. Cotera, W. J. Duschl, F. Melia, & M. J. Rieke ed., *The Central Parsecs of the Galaxy Vol. 186 of Astronomical Society of*

- the Pacific Conference Series, The Galactic Center Black Hole. pp 3–+
- Georgakakis A., Coil A. L., Laird E. S., Griffith R. L., Nandra K., Lotz J. M., Pierce C. M., Cooper M. C., Newman J. A., Koekemoer A. M., 2009, *MNRAS*, 397, 623
- Gilli R., Comastri A., Hasinger G., 2007, *A&A*, 463, 79
- Graham A. W., Driver S. P., 2007, *MNRAS*, 380, L15
- Granato G. L., De Zotti G., Silva L., Bressan A., Danese L., 2004, *ApJ*, 600, 580
- Grogin N. A., Conselice C. J., Chatzichristou E., Alexander D. M., Bauer F. E., Hornschemeier A. E., Jogee S., Koekemoer A. M., Laidler V. G., Livio M., Lucas R. A., Paolillo M., Ravindranath S., Schreier E. J., Simmons B. D., Urry C. M., 2005, *ApJ*, 627, L97
- Gültekin K., Richstone D. O., Gebhardt K., Lauer T. R., Tremaine S., Aller M. C., Bender R., Dressler A., Faber S. M., Filippenko A. V., Green R., Ho L. C., Kormendy J., Magorrian J., Pinkney J., Siopis C., 2009, *ApJ*, 698, 198
- Haardt F., Madau P., 2001, in Neumann D. M., Tran J. T. V., eds, *Clusters of Galaxies and the High Redshift Universe Observed in X-rays Modelling the UV/X-ray cosmic background with CUBA*
- Haehnelt M. G., Rees M. J., 1993, *MNRAS*, 263, 168
- Haiman Z., Loeb A., 1998, *ApJ*, 503, 505
- Häring N., Rix H.-W., 2004, *ApJ*, 604, L89
- Hasinger G., 2004, *Nuclear Physics B Proceedings Supplements*, 132, 86
- Hasinger G., 2008, *A&A*, 490, 905
- Hasinger G., Miyaji T., Schmidt M., 2005, *A&A*, 441, 417
- Heger A., Woosley S. E., 2002, *ApJ*, 567, 532
- Hirschmann M., Khochfar S., Burkert A., Naab T., Genel S., Somerville R. S., 2010, *MNRAS*, 407, 1016
- Hirschmann M., Somerville R. S., Naab T., Burkert A., 2012, *MNRAS*, 426, 237
- Hopkins A. M., Beacom J. F., 2006, *ApJ*, 651, 142
- Hopkins P. F., Hernquist L., Cox T. J., Kereš D., 2008, *ApJS*, 175, 356
- Hopkins P. F., Hernquist L., Cox T. J., Robertson B., Di Matteo T., Springel V., 2006, *ApJ*, 639, 700
- Hopkins P. F., Richards G. T., Hernquist L., 2007, *ApJ*, 654, 731
- Hoyle F., Lyttleton R. A., 1939, *Proceedings of the Cambridge Philosophical Society*, 35, 405
- Hunt M. P., Steidel C. C., Adelberger K. L., Shapley A. E., 2004, *ApJ*, 605, 625
- Ilbert O., Salvato M., Le Floch E., Aussel H., Capak P., McCracken H. J., Mobasher B., Kartaltepe J., Scoville N., Sanders D. B., 2010, *ApJ*, 709, 644
- Jahnke K., Macciò A. V., 2011, *ApJ*, 734, 92
- Jogee S., Miller S., Penner K., Bell E. F., Conselice C., Skelton R. E., Somerville R. S., Rix H., Barazza F. D., 2008, in J. G. Funes & E. M. Corsini ed., *Formation and Evolution of Galaxy Disks Vol. 396 of Astronomical Society of the Pacific Conference Series, Frequency and Impact of Galaxy Mergers and Interactions over the Last 7 Gyr.* pp 337–+
- Johansson P. H., Naab T., Burkert A., 2009, *ApJ*, 690, 802
- Kauffmann G., Haehnelt M., 2000, *MNRAS*, 311, 576
- Kelly B. C., Shen Y., 2013, *ApJ*, 764, 45
- Kelly B. C., Vestergaard M., Fan X., Hopkins P., Hernquist L., Siemiginowska A., 2010, *ApJ*, 719, 1315
- King A., 2005, *ApJ*, 635, L121
- King A., Nixon C., 2013, *ArXiv e-prints*
- Kocevski D. D., Faber S. M., Mozena M., Koekemoer A. M., Nandra K., Rangel C., Laird E. S., Brusa M., Wuyts S., Trump J. R., Koo D. C., Somerville R. S., Bell E. F., Lotz J. M., Alexander D. M., Bournaud F., Conselice C. J., Dahlen T., 2012, *ApJ*, 744, 148
- Kollmeier J. A., Onken C. A., Kochanek C. S., Gould A., Weinberg D. H., Dietrich M., Cool R., Dey A., Eisenstein D. J., Jannuzi B. T., Le Floch E., Stern D., 2006, *ApJ*, 648, 128
- Komatsu E., Smith K. M., Dunkley J., Bennett C. L., Gold B., Hinshaw G., Jarosik N., Larson D., Nolte M. R., Page L., Spergel D. N., Halpern M., 2011, *ApJS*, 192, 18
- Kormendy J., Ho L. C., 2013, *ArXiv e-prints*
- Koushiappas S. M., Bullock J. S., Dekel A., 2004, *MNRAS*, 354, 292
- La Franca F., Fiore F., Comastri A., Perola G. C., Sacchi N., Brusa M., Cocchia F., Feruglio C., Matt G., Vignali C., Carangelo N., Ciliegi P., Lamastra A., Maiolino R., Mignoli M., Molendi S., Puccetti S., 2005, *ApJ*, 635, 864
- La Franca F., Matute I., Fiore F., Gruppioni C., Pozzi F., Vignali C., *The Hellas Elais Consortii 2002*, in R. Maiolino, A. Marconi, & N. Nagar ed., *Issues in Unification of Active Galactic Nuclei Vol. 258 of Astronomical Society of the Pacific Conference Series, The Evolution of AGNs in the Hard X-Rays and the Infrared.* pp 241–+
- Li C., Kauffmann G., Heckman T. M., White S. D. M., Jing Y. P., 2008, *MNRAS*, 385, 1915
- Li Y., Hernquist L., Robertson B., Cox T. J., Hopkins P. F., Springel V., Gao L., Di Matteo T., Zentner A. R., Jenkins A., Yoshida N., 2007, *ApJ*, 665, 187
- Loeb A., Rasio F. A., 1994, *ApJ*, 432, 52
- Lynden-Bell D., 1969, *Nature*, 223, 690
- Madau P., Rees M. J., 2001, *ApJ*, 551, L27
- Magorrian J., Tremaine S., Richstone D., Bender R., Bower G., Dressler A., Faber S. M., Gebhardt K., Green R., Grillmair C., Kormendy J., Lauer T., 1998, *AJ*, 115, 2285
- Maiolino R., Marconi A., Oliva E., 2001, *A&A*, 365, 37
- Maiolino R., Oliva E., Ghinassi F., Pedani M., Mannucci F., Mujica R., Juarez Y., 2004, *A&A*, 420, 889
- Marchesini D., van Dokkum P., Quadri R., Rudnick G., Franx M., Lira P., Wuyts S., Gawiser E., Christlein D., Toft S., 2007, *ApJ*, 656, 42
- Marconi A., Risaliti G., Gilli R., Hunt L. K., Maiolino R., Salvati M., 2004, *MNRAS*, 351, 169
- Marulli F., Bonoli S., Branchini E., Moscardini L., Springel V., 2008, *MNRAS*, 385, 1846
- Matute I., La Franca F., Pozzi F., Gruppioni C., Lari C., Zamorani G., 2006, *A&A*, 451, 443
- Mayer L., Kazantzidis S., Escala A., Callegari S., 2010, *Nature*, 466, 1082
- McCarthy I. G., Schaye J., Bower R. G., Ponman T. J., Booth C. M., Dalla Vecchia C., Springel V., 2011, *MNRAS*, 412, 1965
- McCarthy I. G., Schaye J., Ponman T. J., Bower R. G., Booth C. M., Dalla Vecchia C., Crain R. A., Springel V., Theuns T., Wiersma R. P. C., 2010, *MNRAS*, 406, 822
- McConnell N. J., Ma C.-P., 2013, *ApJ*, 764, 184
- Menci N., Fiore F., Lamastra A., 2013, *ArXiv e-prints*
- Menci N., Fiore F., Perola G. C., Cavaliere A., 2004, *ApJ*, 606, 58

- Miyaji T., Hasinger G., Schmidt M., 2000, *A&A*, 353, 25
- Monaco P., Fontanot F., 2005, *MNRAS*, 359, 283
- Mullaney J. R., Pannella M., Daddi E., Alexander D. M., Elbaz D., Hickox R. C., Bournaud F., Altieri B., Aussel H., Coia D., Dannerbauer H., Dasyra K., 2012, *MNRAS*, 419, 95
- Murray N., Quataert E., Thompson T. A., 2005, *ApJ*, 618, 569
- Nandra K., Laird E. S., Steidel C. C., 2005, *MNRAS*, 360, L39
- Neistein E., Netzer H., 2013, *ArXiv e-prints*
- Padovani P., Matteucci F., 1993, *ApJ*, 416, 26
- Peebles P. J. E., 1965, *ApJ*, 142, 1317
- Peng C. Y., 2007, *ApJ*, 671, 1098
- Pérez-González P. G., Rieke G. H., Villar V., Barro G., Blaylock M., Egami E., Gallego J., Gil de Paz A., Pascual S., Zamorano J., Donley J. L., 2008, *ApJ*, 675, 234
- Pierce C. M., Lotz J. M., Laird E. S., Lin L., Nandra K., Primack J. R., Faber S. M., Barmby P., Park S. Q., Willner S. P., Gwyn S., Koo D. C., Coil A. L., Cooper M. C., Georgakakis A., Koekemoer A. M., Noeske K. G., Weiner B. J., Willmer C. N. A., 2007, *ApJ*, 660, L19
- Richards G. T., Strauss M. A., Fan X., Hall P. B., Jester S., Schneider D. P., Vanden Berk D. E., Stoughton C., Anderson S. F., Brunner R. J., Gray J., Gunn J. E., 2006, *AJ*, 131, 2766
- Robertson B., Bullock J. S., Cox T. J., Di Matteo T., Hernquist L., Springel V., Yoshida N., 2006, *ApJ*, 645, 986
- Robertson B., Hernquist L., Cox T. J., Di Matteo T., Hopkins P. F., Martini P., Springel V., 2006, *ApJ*, 641, 90
- Rosario D. J. e. a., 2012, *A&A*, 545, A45
- Salpeter E. E., 1964, *ApJ*, 140, 796
- Sazonov S. Y., Revnivtsev M. G., 2004, *A&A*, 423, 469
- Schawinski K., Treister E., Urry C. M., Cardamone C. N., Simmons B., Yi S. K., 2011, *ApJ*, 727, L31
- Schulze A., Wisotzki L., 2010, *A&A*, 516, A87+
- Shakura N. I., Sunyaev R. A., 1973, *A&A*, 24, 337
- Shankar F., Marulli F., Mathur S., Bernardi M., Bournaud F., 2012, *A&A*, 540, A23
- Shankar F., Salucci P., Granato G. L., De Zotti G., Danese L., 2004, *MNRAS*, 354, 1020
- Shankar F., Weinberg D. H., Miralda-Escudé J., 2009, *ApJ*, 690, 20
- Shankar F., Weinberg D. H., Shen Y., 2010, *ArXiv:1004.1173*
- Shen Y., Kelly B. C., 2012, *ApJ*, 746, 169
- Sijacki D., Springel V., Di Matteo T., Hernquist L., 2007, *MNRAS*, 380, 877
- Soltan A., 1982, *MNRAS*, 200, 115
- Somerville R. S., Hopkins P. F., Cox T. J., Robertson B. E., Hernquist L., 2008, *MNRAS*, 391, 481
- Springel V., 2005, *MNRAS*, 364, 1105
- Springel V., Di Matteo T., Hernquist L., 2005a, *MNRAS*, 361, 776
- Springel V., Di Matteo T., Hernquist L., 2005b, *MNRAS*, 361, 776
- Springel V., Hernquist L., 2002, *MNRAS*, 333, 649
- Springel V., Hernquist L., 2003, *MNRAS*, 339, 289
- Steffen A. T., Barger A. J., Cowie L. L., Mushotzky R. F., Yang Y., 2003, *ApJ*, 596, L23
- Steinhardt C. L., Elvis M., 2010, *MNRAS*, 402, 2637
- Thielemann F.-K., Argast D., Brachwitz F., Hix W. R., Höflich P., Liebendörfer M., Martínez-Pinedo G., Mezzacappa A., Panov I., Rauscher T., 2003, *Nuclear Physics A*, 718, 139
- Tornatore L., Borgani S., Dolag K., Matteucci F., 2007, *MNRAS*, 382, 1050
- Treister E., Schawinski K., Urry C. M., Simmons B. D., 2012, *ApJ*, 758, L39
- Treister E., Urry C. M., Chatzichristou E., Bauer F., Alexander D. M., Koekemoer A., Van Duyne J., Brandt W. N., Bergeron J., Stern D., Moustakas L. A., Chary R., Conselice C., Cristiani S., Grogin N., 2004, *ApJ*, 616, 123
- Tremaine S., Gebhardt K., Bender R., Bower G., Dressler A., Faber S. M., Filippenko A. V., Green R., Grillmair C., Ho L. C., Kormendy J., Lauer T. R., Magorrian J., Pinkney J., Richstone D., 2002, *ApJ*, 574, 740
- Ueda Y., Akiyama M., Ohta K., Miyaji T., 2003, *ApJ*, 598, 886
- van den Hoek L. B., Groenewegen M. A. T., 1997, *A&AS*, 123, 305
- Vestergaard M., 2003, *ApJ*, 599, 116
- Volonteri M., Haardt F., Madau P., 2003, *ApJ*, 582, 559
- Volonteri M., Stark D. P., 2011, *MNRAS*, 417, 2085
- White S. D. M., Rees M. J., 1978, *MNRAS*, 183, 341
- Wiersma R. P. C., Schaye J., Smith B. D., 2009, *MNRAS*, 393, 99
- Wolf C., Wisotzki L., Borch A., Dye S., Kleinheinrich M., Meisenheimer K., 2003, *A&A*, 408, 499
- Woosley S. E., Weaver T. A., 1995, *ApJS*, 101, 181
- Zel'Dovich Y. B., 1964, *Soviet Physics Doklady*, 9, 195
- Zheng X. Z., Bell E. F., Somerville R. S., Rix H.-W., Jahnke K., Fontanot F., Rieke G. H., Schiminovich D., Meisenheimer K., 2009, *ApJ*, 707, 1566